Prediction of the 3D shape of the L1 vertebral body from adjacent vertebrae

M Sensale, T. Vendeuvre, Arnaud Germaneau, C Grivot, M Rochette, E Dall'Ara

Medical Image Analysis 87 (2023) 102827

Contents lists available at ScienceDirect

Medical Image Analysis

journal homepage: www.elsevier.com/locate/media

Prediction of the 3D shape of the L1 vertebral body from adjacent vertebrae

M. Sensale [a,b], T. Vendeuvre [c,d], A. Germaneau [d], C. Grivot [a], M. Rochette [a], E. Dall'Ara [b,*]

[a] Ansys France, Lyon, France
[b] Department of Oncology and Metabolism, INSIGNEO Institute for in silico Medicine, University of Sheffield, United Kingdom
[c] Spine & Neuromodulation Functional Unit, University Hospital of Poitiers, Poitiers, France
[d] Insitut Pprime UPR 3346 CNRS – Université de Poitiers – ISAE-ENSMA, Poitiers, France

ARTICLE INFO

Keywords:
Vertebral fractures
CT-scan images
Statistical shape modeling
Shape prediction

ABSTRACT

The aim of treatments of vertebral fractures is the anatomical reduction to restore the physiological biomechanics of the spine and the stabilization of the fracture to allow bone healing. However, the three-dimensional shape of the fractured vertebral body before the fracture is unknown in the clinical setting. Information about the pre-fracture vertebral body shape could help surgeons to select the optimal treatment. The goal of this study was to develop and validate a method based on Singular Value Decomposition (SVD) to predict the shape of the vertebral body of L1 from the shapes of T12 and L2.

The geometry of the vertebral bodies of T12, L1 and L2 vertebrae of 40 patients were extracted from CT scans available from the VerSe2020 open-access dataset. Surface triangular meshes of each vertebra were morphed onto a template mesh. The set of vectors with the node coordinates of the morphed T12, L1 and L2 were compressed with SVD and used to build a system of linear equations. This system was used to solve a minimization problem and to reconstruct the shape of L1. A leave-one-out cross-validation was performed. Moreover, the approach was tested against an independent dataset with large osteophytes.

The results of the study show a good prediction of the shape of the vertebral body of L1 from the shapes of the two adjacent vertebrae (mean error equal to 0.51 ± 0.11 mm on average, Hausdorff distance equal to 2.11 ± 0.56 mm on average), compared to current CT resolution typically used in the operating room. The error was slightly higher for patients presenting large osteophytes or severe bone degeneration (mean error equal to 0.65 ± 0.10 mm, Hausdorff distance equal to 3.54 ± 1.03 mm). The accuracy of the prediction was significantly better than approximating the shape of the vertebral body of L1 by the shape of T12 or L2. This approach could be used in the future to improve the pre-planning of spine surgeries to treat vertebral fractures.

1. Introduction

Vertebral fractures are a widespread disease that can cause acute and chronic pain, deterioration of the quality of life and reduction of the life span. Traumatic vertebral fractures can occur due to high-energy events (e.g. falls, car accidents etc.) as well as after routine daily activities such as lifting (Schousboe, 2016). In the US an annual incidence of about 160,000 traumatic vertebral fractures per year has been reported (Grazier et al., 1984). As the population increased over the last forty years, those figures underestimate the real number of traumatic vertebral fractures in current years. The incidence of traumatic vertebral fractures is highest at the thoracolumbar junction, and L1 is the most recurrent fractured level (30% of all fractures) followed by T12 (18%) and L2 (13%) (Wang et al., 2020). The anatomical reduction of the fracture and the restoration of the vertebral body shape are crucial objectives of surgical treatments, as they result in re-establishing the natural curvature of the spine, improving the biomechanics of the segment and relieving pain (AOSpine association (Aebi, 2007)). This is especially important for individuals who are young or middle-aged and desire to resume the active lifestyles they had before the fracture. In order to perform a biomechanical stable anatomical reduction of the vertebral body, surgeons can choose among different treatments, without, however, any real consensus regarding the type of surgery (Verheyden et al., 2018). including posterior fixation, anterior stabilization, etc. (Vaccaro et al., 2020). Traumatic thoracolumbar fractures have been treated by posterior fixation or anterior stabilization (Vaccaro et al., 2020), and also by posterior fixation in combination with balloon kyphoplasty (Salle et al., 2021) as well as with balloon kyphoplasty alone (Maestretti et al.,

* Corresponding author at: Pam Liversidge Building, Sheffield, S1 3JD
E-mail address: e.dallara@sheffield.ac.uk (E. Dall'Ara).

https://doi.org/10.1016/j.media.2023.102827
Received 8 April 2022; Received in revised form 14 April 2023; Accepted 18 April 2023
Available online 20 April 2023

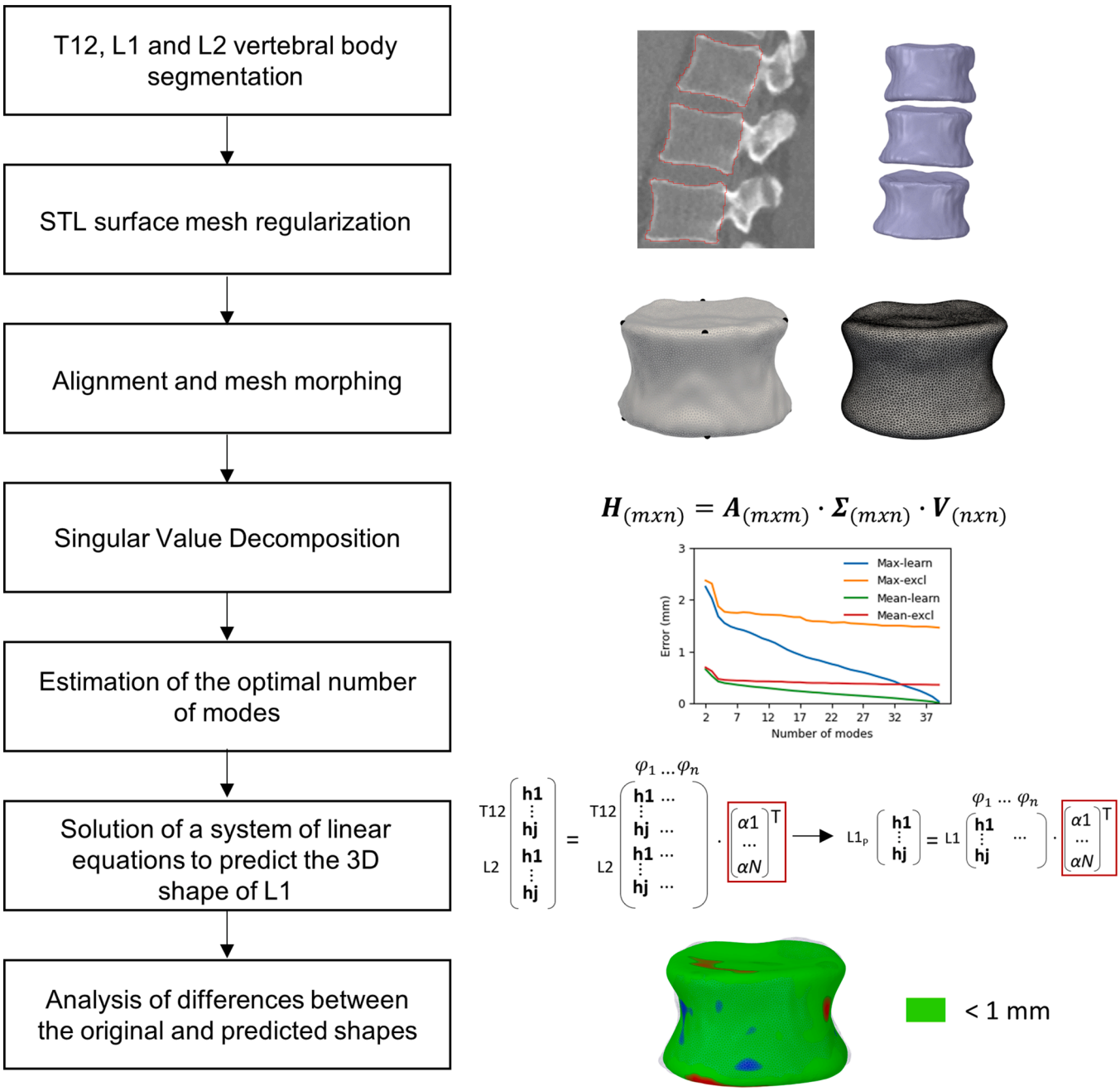

Fig. 1. An overview of the different steps to predict the 3D shape of the L1 vertebral body by using the 3D shapes of the two adjacent vertebral bodies.

2014). Balloon kyphoplasty is an effective surgery to restore the vertebral body height and local kyphotic angulation (Van Meirhaeghe et al., 2013). Although restored vertebral height has been shown, fractured endplate reduction is somewhat limited and might result in various disk healing and modification patterns, which could lead to problems including recurring pain, kyphosis and adjacent compression fractures (Lin et al., 2009; Ortiz and Bordia, 2011). A more thorough approach should examine not only the sagittal alignment of the spine but also the anatomical restoration of the vertebral body geometry as a whole, including the cortical ring and endplates, treating vertebral joint injuries as other injuries involving weight-bearing joints (Noriega González et al., 2022). In this regard, a technique based on expandable titanium implants positioned below the fracture and cement injection has been shown successfully on a few cases demonstrating a new trend towards an anatomical 3D reduction of vertebral fractures (Noriega González et al., 2022).

The information about the 3D shape of the fractured vertebra before the fracture could be used during the pre-operative planning to aid surgeons in the choice of the most suited surgery, or during the surgery as a benchmark to perform the anatomical reduction of the fracture as a whole. However, the original 3D shape of the fractured vertebra is often not known to the surgeon in the pre-operative setting.

Statistical shape models (SSMs) can represent the possible variations in shape of an object belonging to a specific population and have often been applied to the spine. SSMs of the spine have been used to describe the geometric variation in spinal curvature (Hollenbeck et al., 2018) and single vertebrae (Clogenson et al., 2015). Recent developments have increased the ability of SSMs to segment vertebrae (Pereañez et al., 2015). Other applications of SSMs of the spine are fracture detection (Roberts et al., 2010), 2D-to-3D reconstruction from DXA images (Zheng et al., 2011; Whitmarsh et al., 2013), automatic generation of finite element models (Campbell and Petrella, 2016, Campbell and

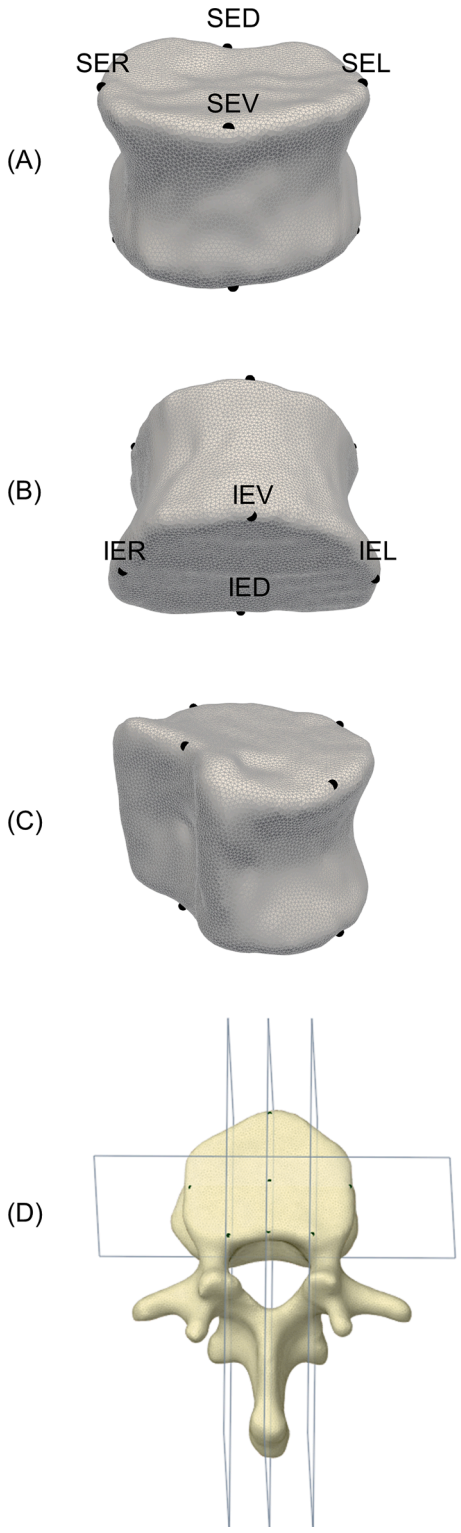

Fig. 2. Anatomical landmarks placed on the superior and inferior endplates of the vertebral bodies, for Patient #33, on T12 (A), L1 (B) and L2 (C) in cranial-frontal, caudal-frontal, postero-lateral views, respectively. Anatomical planes to define the landmarks on the superior endplate (D), the anatomical planes to define the landmarks on the inferior endplate were similar.

Petrella, 2015) and automatic creation of image-based finite element models including material properties (Day et al., 2022). However, these SSMs have never been applied to the reconstruction of the premorbid shape of a vertebra. Recently, different studies assessed the potential of SSMs to reconstruct the premorbid shape of a bone such as the cranial vault (Fuessinger et al., 2018) the mandible (Wang et al., 2021), the scapula (Plessers et al., 2018; Salhi et al., 2020) and the acetabulum (Vanden Berghe et al., 2017). In these studies, SSMs were used to virtually reconstruct the shape of the bone after some defects were artificially created to simulate a pathologic condition. The predicted shape was compared with the original one to assess the performance of the method by evaluating distance metrics between the meshes. These approaches were associated with low reconstruction errors (mean reconstruction error of about 1 mm (Salhi et al., 2020; Vanden Berghe et al., 2017)), and were considered applicable for pre-surgery planning or biomechanics modeling pipelines. If the contralateral bone was used as a template for the reconstruction, higher reconstruction errors (12% to 26% higher) were found (Krol et al., 2013; Vanden Berghe et al., 2017).

However, these approaches have seldom been applied to the spine. SSMs were employed by de Bruijne et al. (2007) for vertebral fracture quantification from 2D X-ray images. In particular, conditional shape models were used to predict the shape of one lumbar vertebra based on the shapes of other adjacent vertebrae (L1-L4). To validate the approach, it has been applied to 282 X-ray images, showing a mean ($\pm$ standard deviation) distance between the original and reconstructed 2D shapes equal to 0.8 ± 0.4 mm. Nevertheless, the main limitation of this method is the application to the 2D sagittal X-ray images, which do not provide a reliable shape of the whole vertebral body and were associated with low inter-observer reproducibility for the measurement of vertebral height based on six anatomical landmarks (Genant et al., 1993). The usage of Computed Tomography (CT) scans, often integrated in clinical protocols, has the potential of improving the assessment of the 3D geometry of the pre-fracture shape of the vertebral body using SSMs, but needs further development and validation.

The aim of this study was to develop and validate a method to predict the 3D shape of the L1 vertebral body from the shapes of the adjacent T12 and L2 vertebral bodies, estimated by individual segmentations of CT images.

2. Materials and methods

2.1. Summary

An overview of the study is shown in Fig. 1. Briefly, the segmentation of T12, L1 and L2 vertebral bodies from CT scans of 40 patients were processed. An average reference template mesh was generated and the mesh of each vertebra was aligned and morphed onto that reference mesh. The vectors of node coordinates of the morphed meshes were compressed by Singular Value Decomposition (SVD). An optimal set of modes was used to build a linear system of equations to predict the 3D shape of the L1 by considering only the information corresponding to T12 and L2. A leave one out cross-validation was performed and the accuracy of the validated approach was tested with an independent dataset. The accuracy of the approach was evaluated by comparing the predicted and real mesh of L1.

2.2. Dataset construction

The publicly available VerSe2020 database of CT-scan images and segmentation masks was used in this study (Kirschke et al., 2020; Liebl et al., 2021; Löffler et al., 2020; Sekuboyina et al., 2020). A subgroup of 40 patients from the database was processed for model construction. Patients were randomly picked from the database (22 men, 18 women; ID numbers of patients in the VerSe2020 database are reported in Appendix A). Exclusion criteria were severe bone degeneration (e.g., marked asymmetries along the antero-posterior or right-left directions), presence of large osteophytes (e.g., osteophytes that bridge between different vertebral levels or osteophytes at the level of the endplates), fractures or signs of previous fractures at T12, L1 or L2 levels, as

Table 1
Name, abbreviation and anatomical definition of the 8 landmarks placed on the superior and inferior endplates of each vertebral body.

Name	Abb.	Definition
Superior Endplate Ventral	SEV	Cranial to caudal view, consider the sagittal plane that cuts the superior endplate in two halves, consider the most ventral point on the superior endplate
Superior Endplate Dorsal	SED	As SEV but consider the most dorsal point
Superior Endplate Right	SER	Cranial to caudal view, back to front view, consider the coronal plane that cut the superior endplate in two halves, consider the rightmost point on the superior endplate
Superior Endplate Left	SEL	As SER but consider the most left point
Inferior Endplate Ventral	IEV	Caudal to cranial view, consider the sagittal plane that cut the inferior endplate in two halves, consider the most ventral point on the inferior endplate
Inferior Endplate Dorsal	IED	As IEV but consider the most dorsal point
Inferior Endplate Right	IER	Caudal to cranial view, back to front view, consider the coronal plane that cut the inferior endplate in two halves, consider the rightmost point on the inferior endplate
Inferior Endplate Left	IEL	As IER but consider the most left point

Table 2
Size of the vertebrae within the testing dataset reported as antero-posterior width (Width-AP), left-right width (Width-LR) and height.

Vertebral level	Construction dataset Width-AP (mm)		Width-LR (mm)		Height (mm)	
	Avg ± st dev	(Min, Max)	Avg ± st dev	(Min, Max)	Avg ± st dev	(Min, Max)
T12	29.6 ± 3.15	(23.4, 35.2)	39.8 ± 3.98	(30.7, 46.9)	24.6 ± 1.96	(20.4, 28.8)
L1	30.4 ± 2.97	(24.0, 35.7)	41.6 ± 4.12	(33.5, 49.4)	26.0 ± 1.95	(21.6, 30.5)
L2	32.1 ± 3.30	(26.0, 37.7)	43.5 ± 4.15	(36.9, 52.3)	26.6 ± 1.92	(22.7, 31.2)
T12, L1 and L2	30.7 ± 3.31	(23.4, 37.7)	41.5 ± 4.42	(30.7, 52.3)	25.8 ± 2.14	(20.4, 31.2)
	Testing dataset Width-AP (mm)		Width-LR (mm)		Height (mm)	
Vertebral level	Avg ± st dev	(Min, Max)	Avg ± st dev	(Min, Max)	Avg ± st dev	(Min, Max)
T12	28.2 ± 2.02	(25.1, 30.6)	39.5 ± 1.95	(36.7, 42.4)	23.2 ± 1.57	(21.0, 25.5)
L1	29.1 ± 2.16	(25.4, 31.2)	42.2 ± 2.49	(39.5, 46.9)	24.7 ± 1.17	(23.2, 26.5)
L2	31.1 ± 3.22	(25.8, 35.9)	44.7 ± 1.76	(42.0, 47.4)	24.8 ± 0.62	(23.9, 25.7)
T12, L1 and L2	29.4 ± 2.80	(25.1, 35.9)	42.0 ± 2.91	(36.7, 47.4)	24.3 ± 1.38	(21.0, 26.5)

pathologic bones are not suited to the creation of SSMs. As a result, the mean age of patients within the dataset was 40.9 ± 15.9 years (18.9 – 77 years) that matches well the target population that would benefit from this study (i.e. those suffering of traumatic fractures). The CT voxel size was variable, from $0.68\times0.68\times0.45$ mm^3 to $1.31\times1.31\times3$ mm^3 (Appendix A). An additional subset of 5 patients from the database (Testing dataset) was used to test the validated approach with an independent dataset (Patient #40 to Patient #45). Among those patients, three presented large osteophytes and severe bone degeneration (Appendix A).

For each mesh of the dataset, eight anatomical landmarks were placed on the superior and inferior endplates (Fig. 2) (Yeung et al., 2020). The instructions to retrieve the anatomical position of the landmarks are reported in Table 1. Based on anatomical landmarks, the height and width of each vertebra was calculated and are reported in Table 2. To calculate the height, least-squares planes fitting landmarks on the superior and inferior endplates were calculated. A sagittal direction was estimated as the average of the normal to the two planes. The landmarks were projected onto a line parallel to the sagittal direction and going through the center of mass of the landmarks. The height was estimated as the mean distance between projected landmarks on the superior and the inferior endplates. To calculate the width, landmarks were first projected onto the least-squares planes. Then, by using projected landmarks, an antero-posterior width was calculated as the average of the distance between SED and SEV and the distance between IEV and IED; a lateral width was calculated as the average of the distance between SER and SEL and the distance between IER and IEL.

2.3. Image segmentation for vertebral bodies

From the segmented images of the vertebra, the geometry of the vertebral body was obtained with a manual procedure as following (3DSlicer, v4.11.0) (Fedorov et al., 2012). The posterior part of the vertebra was cut from the cross sections by considering the contours of the endplates as boundaries of the vertebral body. Once the vertebral bodies were isolated, the segmented images were smoothed with a Gaussian smoothing filter (standard deviation of 0.8 mm). Each vertebral body was overlapped with the CT-scan images to qualitatively assess the extraction of proper geometry. Manual corrections were performed to segmented images in case adjustments were required. An example of the segmented geometry overlapped to the CT images is showed in Fig. 3. A surface mesh was generated from each segmentation, followed by a regularization with an element size of 0.4 mm.

2.4. Mesh morphing

The methods used for the mesh morphing of the vertebral bodies and the construction of a set of isotopological surface meshes (same number of nodes, same number of elements, same connectivity, preserved topology-anatomy correspondence) are based on Gaussian process (GP) morphable models implemented in Scalismo software (Scalismo, version 0.90, Graphics and Vision Research group, University of Basel, 2020; Luthi et al., 2018) and are detailed in the next sections. An overview of

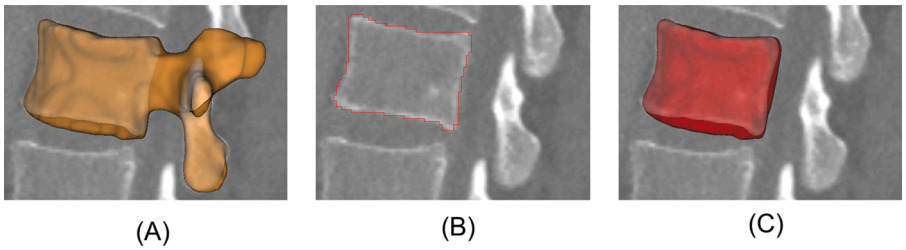

Fig. 3. Example of segmentation for Patient #5 (L1) in a sagittal view: 3D representation of the whole vertebra (A); segmentation mask of the vertebral body (B); 3D representation of the segmented vertebral body (C).

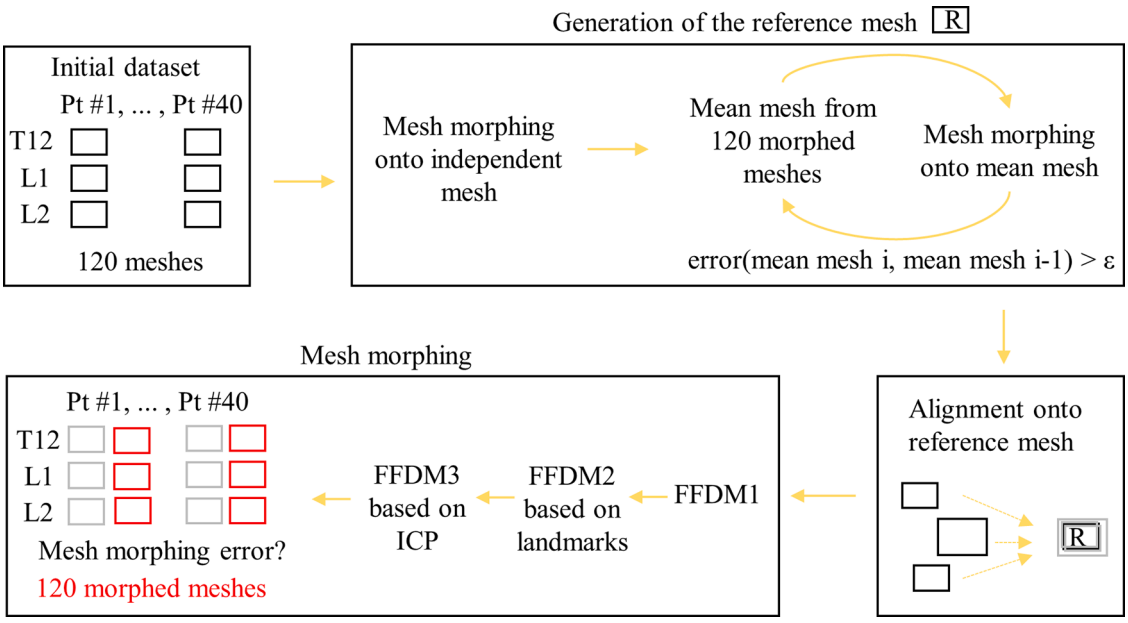

Fig. 4. Mesh morphing workflow. The starting point is the set of 120 meshes of the vertebral bodies of 40 patients (Patient #1 to Patient #40). From this set of meshes and through an iterative procedure (ε represents the threshold error), an optimal reference mesh is generated. The set of meshes is aligned onto the reference mesh (R) and the reference mesh is morphed onto each geometry in order to obtain a new set of geometries with the same number of nodes and elements, and same connectivity. The morphed meshes are obtained from a three steps procedure where a free-form deformation model (FFDM1) is created from the reference mesh, then adapted to each geometry based on displacements between anatomical landmarks (FFDM2) and between points sampled on the meshes in an Iterative closest point (ICP) process (FFDM3).

the different steps to obtain morphed meshes is presented in Fig. 4.

2.4.1. Generation of the reference mesh

A reference mesh was generated through an iterative procedure to avoid biasing the accuracy of the mesh morphing to a particular vertebra. To initialize the process, an independent reference mesh with an element size of 0.7 mm and about 12,000 nodes was morphed onto the 120 geometries (T12, L1 and L2 vertebral bodies for each patient). This element size has been chosen lower than the one of target meshes to reduce the computational time. A mean mesh was calculated from the 120 morphed geometries and used as reference mesh in the first step of an iterative mesh morphing process. At each iteration, the mesh morphing of the 120 geometries onto the mean mesh was done by using the mesh morphing algorithm described below, then a new mean mesh was computed and compared with the mean mesh of the previous iteration. As metrics to compare two meshes, the mean error with respect to the target mesh (Eq. (1)) and the Hausdorff distance (HD) (Eq. (2)) were considered:

$$Mean\ error\ = 1/N \sum_{j=1}^{J} dist\left(h_j,\ S_{target}\right) \tag{1}$$

$$Hausdorff\ distance\ (HD) = \max\left\{max\left\{dist\left(h_{morphed},\ S_{target}\right)\right\};\ max\left\{dist\left(h_{target},\ S_{morphed}\right)\right\}\right\} \tag{2}$$

where: N is the number of nodes of the morphed mesh, $\mathbf{h}_j$ is the j-node of the morphed mesh, $\mathbf{S}_{target}$ is the target mesh; $\mathbf{h}_{morphed}$ and $\mathbf{h}_{target}$ are the nodes of the morphed and target meshes $\mathbf{S}_{morphed}$ and $\mathbf{S}_{target}$, *dist* is the Euclidean distance. The point-to-cell distance was calculated by performing a geometric interpolation of the cells of the surface mesh (Commandeur et al., 2011; Schroeder et al., 2006). In fact, the algorithm computes the minimum distance between each point of the morphed mesh and each point belonging to the surface that interpolates the closest element of the target mesh. The iterative process was stopped when the HD between the mean mesh at iteration (*i*) and the mean mesh at iteration *(i-1)* was lower than 0.12 mm, which is more than three times lower than the voxel size of the CT-scan with the best resolution in the dataset (approximately 0.45 mm^3)The mean distance and the HD between the mean mesh at the (*i*)-iteration and the mean mesh at the *(i-1)*-iteration are reported in function of the number of iterations (Fig. 5A). The mean mesh at iteration 1 was compared to the independent reference mesh. The mean mesh at iteration 3 was considered acceptable as the reference mesh for the mesh morphing (Fig. 5B-C). Iteration 4 must be considered as a confirmation of the choice of the mean mesh at iteration 3. We verified that the average mesh morphing error (mean error and Hausdorff distance) did not change between iterations 2 and 4.

2.4.2. Alignment

The best rigid transformation that minimizes the distance between the position of landmarks on the reference mesh and the position of landmarks on the morphed mesh after the transformation was identified. The minimization problem was solved with a linear least squares method. A routine in Scalismo (Scalismo, version 0.90; Graphics and Vision Research group, University of Basel, 2020; Luthi et al., 2018) was used for the alignment. As a consequence, the pose of the vertebrae was not considered in this study.

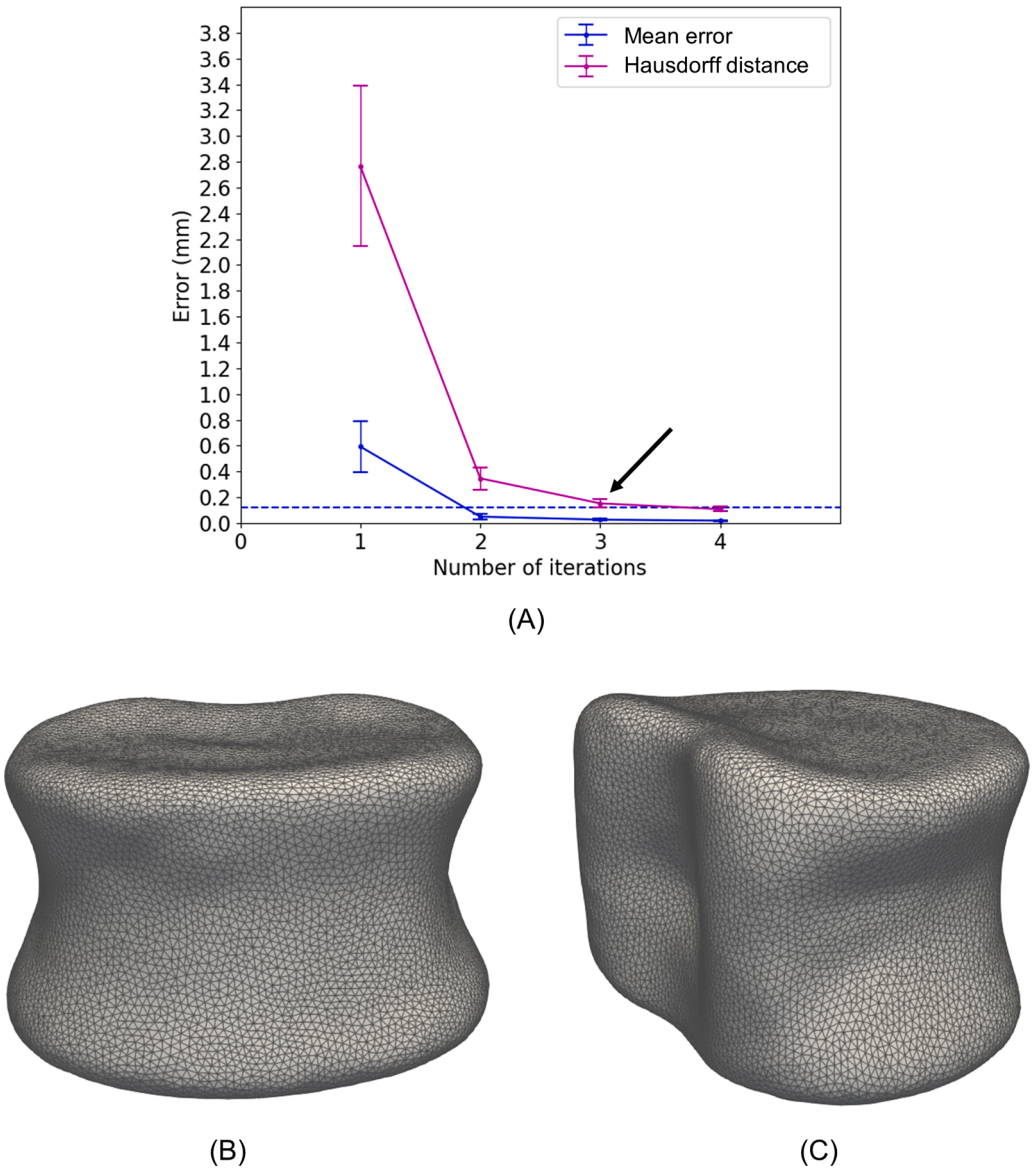

Fig. 5. Mean error and Hausdorff distance (HD) (mm) between the mean mesh calculated at iteration (i) and the mean mesh calculated at iteration (i-1) (A). The dash-dotted line represents the threshold error of 0.12 mm. The mean mesh at iteration 3 was considered as reference mesh for further analyses as the HD with the mean mesh at iteration 4 was below the threshold error, and it is showed in frontal (B) and posterolateral (C) view.

2.4.3. Deformable morphing algorithm

Based on the reference mesh, a deformable model was built with a GP and morphed onto the dataset of aligned meshes. A low-rank approximation of the GP characterised by a set of mode deformations of the reference mesh was used. The coefficients of these deformation modes were optimised to deform the reference mesh so that it matched the target shapes in the dataset.

The reference mesh was chosen as the mean mesh of the GP, and a combination of two multi-scale Gaussian kernels was used. Gaussian kernels are able to enforce smooth deformations, and, in their scalar-valued form, are defined as:

$$k_g = e^{-\frac{\|x-y\|^2}{\sigma^2}} \tag{3}$$

where the parameter σ is associated with the degree of smoothness of the deformation field (Luthi et al., 2018). The first kernel took into account global shape variations of the geometry ($\sigma = 50$) while the second considered more localised changes ($\sigma = 5$). A finite-rank approximation of the GP was computed with a rank (i.e. the number of basis functions of the GP) equal to 200. This was done by using the Nystrom method (Luthi et al., 2018) with 1500 uniformly sampled points. These settings were chosen after preliminary analyses to optimize the mesh morphing outcome. This free-form deformation model (FFDM1) allows modeling of an ideally infinite range of non-meaningful deformations of the reference vertebra.

Then, for each mesh in the dataset, the displacements between the anatomical landmarks placed on the reference mesh and the landmarks on the target mesh were incorporated within the FFDM1 through a GP regression, giving a so-called posterior model (FFDM2). Thanks to this process, the variance of the FFDM1 was constrained and the FFDM2 was able to represent more meaningful shapes than those obtained from the FFDM1. The same landmarks used for the alignment were used also for the creation of the FFDM2 (Fig. 2).

The FFDM2 was morphed onto the target mesh with an iterative process based on displacements between regularly sampled points on the reference mesh and the respective closest points evaluated on the target mesh (Salhi et al., 2020). This GP regression, based on a large number of points, results in a highly constrained GP that represents a full

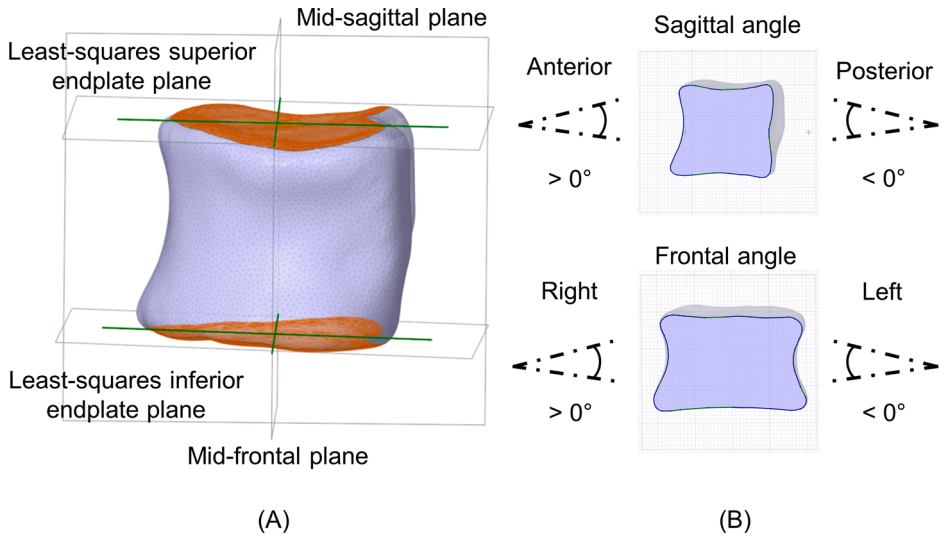

Fig. 6. Anatomical planes (A) used to define sagittal and frontal angles (B).

normal distribution of shapes fitting the target shape (FFDM3). The mean mesh of the FFDM3 represents the final morphed mesh. The closest points on the target mesh were evaluated in an iterative process to improve the fitting (Iterative Closest Point, ICP). The mesh morphing process was characterized by the following steps:

1 10,000 sample nodes were sampled on the reference mesh covering regularly the whole geometry
2 For each of those nodes, the closest point on the target mesh was selected as candidate correspondence
3 The displacements between the sample nodes on the reference mesh and the candidate correspondences on the target geometry were incorporated within the FFDM2 through a GP regression. This allowed to obtain the FFDM3
4 The spatial position of the 10,000 nodes previously sampled was computed on the FFDM3 from the previous step, and the closest points on the target mesh were selected as candidate correspondences
5 The displacements between the sample nodes on reference mesh and the new candidate correspondences identified in the previous step were incorporated within the FFDM2 through a GP regression. This approach allowed a new FFDM3 based on a better estimation of the closest points, and therefore a new morphed mesh, to be obtained.
6 Loop to step 4 to update the displacements used in the GP regression based on the new morphed mesh and repeat for 100 iterations.

At the end of this iterative procedure, to evaluate the accuracy of the algorithm, the mean error and HD were considered between the morphed meshes and the original geometries.

2.5. Prediction of the shape of L1

For each patient, a vector **h** with the coordinates of the nodes of the morphed T12, L1 and L2 surface meshes was created. The set of vectors for patients in the dataset for model construction was compressed by SVD. A leave-one-out experiment was performed for each number of modes (from 2 to 38 modes) in order to estimate the optimal number of modes to describe the variability of the geometries within the dataset (Xu and Goodacre, 2018). For a fixed number of modes (**k**), one vector was left-out and the remaining 39 vectors were compressed with SVD keeping the first **k** modes:

$$H_{(mxn)} = A_{(mxm)} \cdot \Sigma_{(mxn)} \cdot V_{(nxn)} \tag{4}$$

where **H** is the matrix where the columns are the vectors **h** of node coordinates of each patient, **A** is composed of the left singular vectors (modes) of **H, Σ** is a diagonal matrix composed of the singular values σ_k of **H, V** is composed of the right singular vectors of **H**, m is equal to three times the number of node coordinates of a morphed vertebra, *n* is equal to 39.

Each basis of **k** modes was assessed to evaluate the accuracy of the representation of the left-out vector and the learning vectors. Each vector was projected in the basis of **k** modes, and the surface mesh of T12, L1 and L2 was reconstructed from the projected vector. These meshes were compared with the morphed and original meshes based on the mean error and HD as described above. The error associated with L1 alone and the average error associated with T12, L1 and L2 were evaluated. The error for the left-out patient and mean error for the 39 learning patients were assessed. This was repeated for each patient, therefore 40 different bases were built for any fixed **k**. As output of the leave-one-out experiment, the average errors among the 40 bases, evaluated on the left-out patients or on the learning patients (only on L1 or averaged over the three vertebrae), were calculated to define the optimal number of modes.

Once the optimal **k** was fixed and the modes were extracted, the leave-one-out experiment was repeated to validate the method that aims to predict the shape of L1 from the shapes of T12 and L2 (Plessers et al., 2018; Salhi et al., 2020; Vanden Berghe et al., 2017; Wang et al., 2021). This method was based on a minimization problem. Briefly, each vector including the node coordinates of the morphed vertebral bodies could be approximated as a linear combination of the modes as:

$$h_{proj} = A \cdot \alpha \tag{5}$$

where **α** is a vector of **k** parameters.

Given a patient not belonging to the dataset and for which the node coordinates corresponding to the L1 level are not available, we hypothesize that the corresponding vector of node coordinates of T12 and L2 levels $\mathbf{h}_{T12\text{-}L2}$ could be approximated as a linear combination of modes related to the T12 and L2 parts of the matrix as:

$$h_{T12-L2\ proj} = A_{T12-L2} \cdot \alpha \tag{6}$$

where $\mathbf{A}_{T12\text{-}L2}$ is the part of the matrix **A** that includes only the node coordinates of T12 and L2 of the **k** modes, and **α** is a vector of **k** parameters. As the columns of $\mathbf{A}_{T12\text{-}L2}$ are linearly independent, the linear-least-square (LLS) solution **α'** of this system is unique. The following minimization problem was solved:

$$\boldsymbol{\alpha}' = \underset{\boldsymbol{\alpha} \in \mathbb{R}^k}{\mathbf{argmin}} \parallel \boldsymbol{h}_{T12-L2\ proj} - \boldsymbol{h}_{T12-L2} \parallel \tag{7}$$

Table 3
Mean error and Hausdorff distance (HD) (mm) between the morphed mesh and the original geometry, averaged over all the patients, for T12, L1 and L2 levels, and averaged over the three levels. * represents a significant difference in the mean error or in the HD for the T12 or L2 vertebrae compared to the L1 vertebra.

Vertebral level	Mean error (mm)		Hausdorff distance (mm)	
	Average ± st dev	(Min, Max)	Average ± st dev	(Min, Max)
T12	*0.140 ± 0.023	(0.093, 0.180)	1.030 ± 0.360	(0.556, 2.165)
L1	0.135 ± 0.018	(0.099, 0.177)	0.886 ± 0.205	(0.599, 1.628)
L2	*0.142 ± 0.022	(0.103, 0.188)	0.961 ± 0.311	(0.478, 1.901)
T12, L1 and L2	0.139 ± 0.021	(0.093, 0.188)	0.959 ± 0.301	(0.478, 2.165)

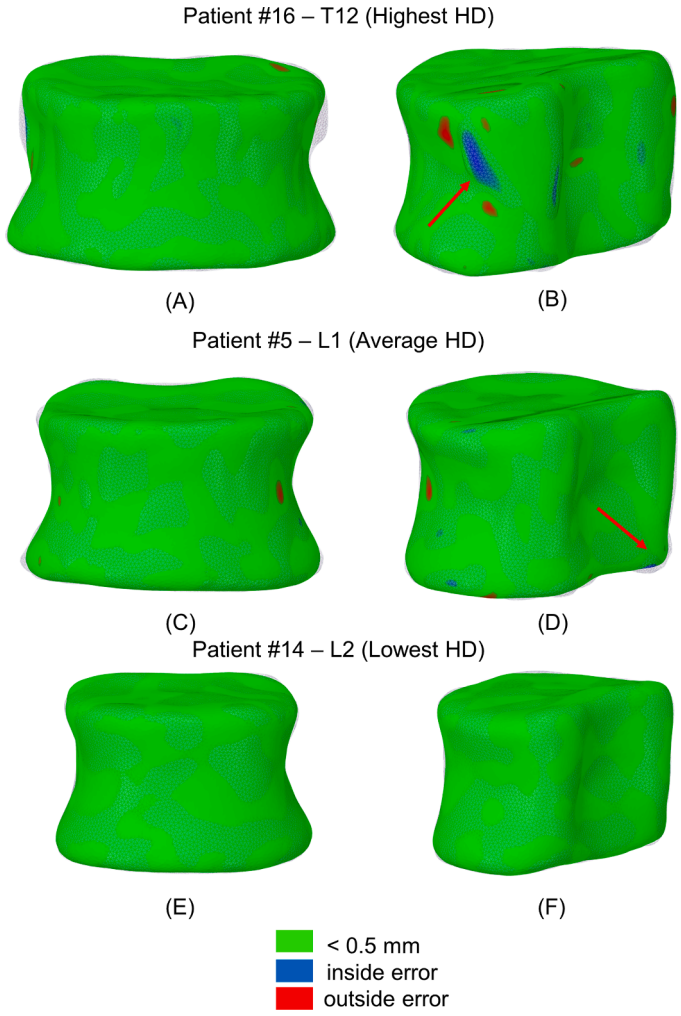

Fig. 7. Frontal and posterolateral views of the spatial distribution of the error between morphed and original meshes for the highest (A-B), average (C-D) and lowest (E-F) Hausdorff distance (HD). Red arrows indicate the area where the HD occurred. The error is considered "inside" when the morphed mesh is inside the original one, and "outside" when the morphed mesh is outside the original one. Errors lower than 0.5 mm (value closest close to the voxel size of the best CT-scan) are reported in green.

where $\|\cdot\|$ is the Euclidean norm. Then, we hypothesize that the coefficients $\boldsymbol{\alpha}$' can be used to reconstruct the vector of node coordinates of L1 ($\mathbf{h}_{L1}$) as:

$$h_{L1} = A_{L1} \cdot \alpha' \tag{8}$$

where $\mathbf{A}_{L1}$ is the part of the matrix $\mathbf{A}$ that includes only the node coordinates of L1 of the $\mathbf{k}$ modes.

For each left-out patient, the mean error and HD were calculated. For patients presenting the highest, the lowest and average mean error and HD, the distribution of heights of the predicted surface mesh of the L1 vertebral body and the respective original mesh were overlapped and compared. The heights were consistently defined along an average cranio-caudal direction between triangles of the superior endplate and points intersecting the inferior endplate. A heatmap of the distribution of heights was computed by using a linear interpolator and a step size of 0.7 mm (equal to the average size of triangles). Also, frequency plots of the distribution of heights and the median values were calculated. For the same patients, sagittal and frontal angles between the endplates were calculated based on the original and predicted geometries (Fig. 6). Vertebral endplates were defined manually on the original and predicted geometries. First, anatomical landmarks used in the mesh morphing algorithm (Table 1) were used to define the antero-posterior and right-left limits of the endplates. Secondly, four lines were drawn on each endplate to join the landmarks and isolate the endplates. The angles were defined in the mid-sagittal and mid-frontal planes based on least-squares planes fitting the endplates. Anterior and right angles were considered positive (Fig. 6B). The difference between angles measured on original or predicted geometries was defined as absolute difference if angles were both anterior (posterior) or right (left), or as the sum of the absolute values of the angles if they were of different sign.

The minimization was repeated to simulate the cases when only T12 or only L2 were available. Therefore, the following systems of linear equations were considered and solved with a LLS method:

$$h_{L2} = A_{L2} \cdot \alpha \tag{9}$$

$$h_{T12} = A_{T12} \cdot \alpha \tag{10}$$

where $\mathbf{A}_{L2}$ is the part of the matrix $\mathbf{A}$ that includes only the node coordinates of L2 of the $\mathbf{k}$ modes, $\mathbf{A}_{T12}$ is the part of the matrix $\mathbf{A}$ that includes only the node coordinates of T12 of the $\mathbf{k}$ modes. For each left-out patient, the mean error and HD between the predicted surface mesh of L1 and the respective original meshes were evaluated.

The method to predict the shape of L1 was also tested on an independent dataset of 5 patients (see Section 2.2). For each patient, the mean error and HD were calculated, as well as the distribution of heights for both predicted and real meshes, frequency plots of the distribution of heights, and sagittal and frontal angles between the endplates.

2.6. Comparison with simpler approach

The estimation of the shape of the L1 vertebral body was compared with the results from a simpler algorithm that uses the segmented shapes of the T12 or L2 vertebral bodies. The mean error and HD were calculated by comparing T12 (real) and L1 (real) or L2 (real) and L1 (real). The results were then compared to the SSM approach presented above.

2.7. Statistical analyses

Descriptive statistics were used to investigate: the influence of the vertebral level (variable assuming values T12, L1 or L2) on the mesh morphing error; the influence of the number of levels used to compute the prediction of L1 (T12+L2, T12 only or L2 only) on the reconstruction error; any difference between the reconstruction error evaluated with respect to the original or morphed meshes; any difference between the reconstruction error of L1 and the projection error obtained for the number of modes $\mathbf{k}$ used to predict the shape of the L1 vertebral body.

The normality of data was tested through a Kolmogorov-Smirnoff test. The sphericity of data was tested through a Mauchly's test. In

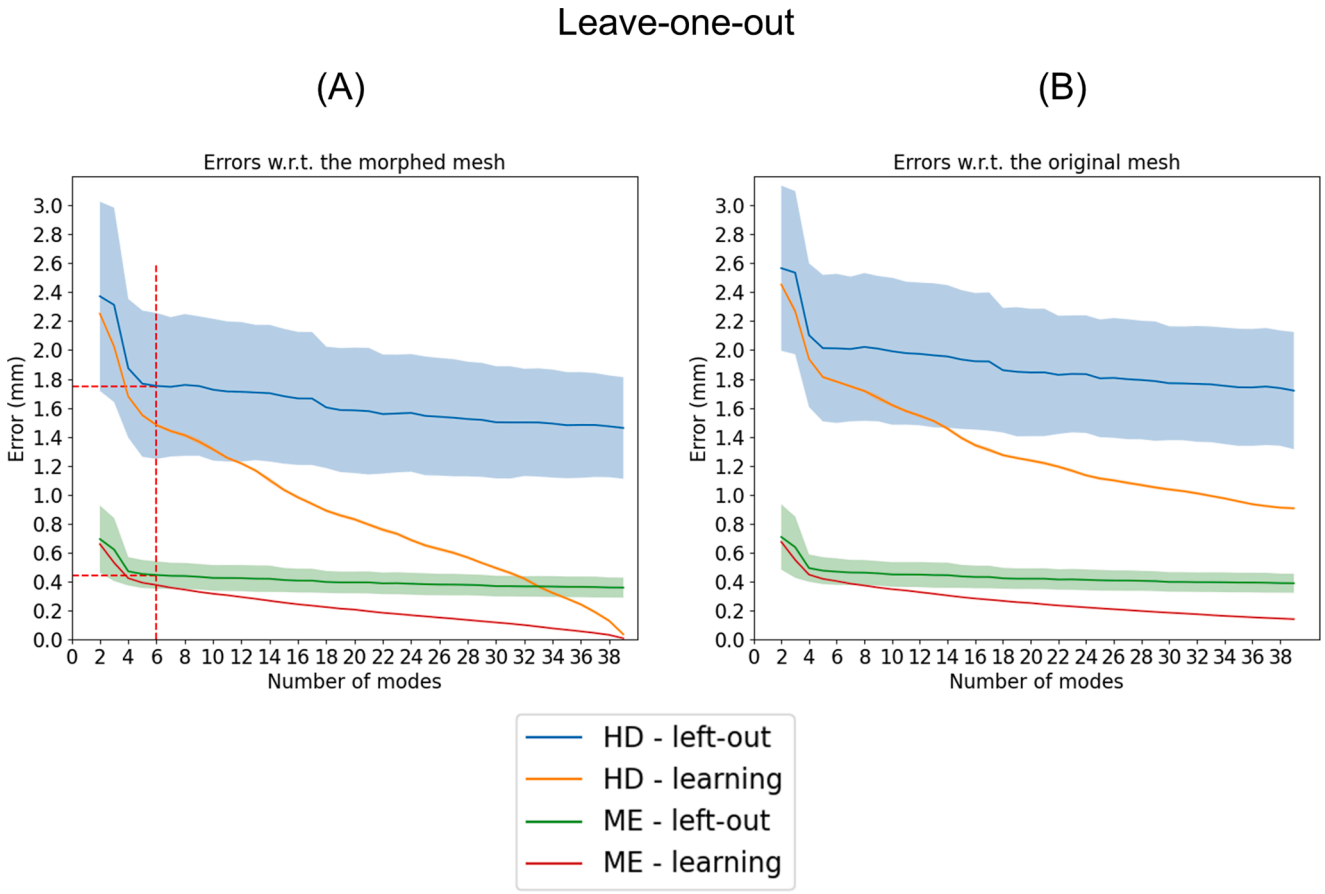

Fig. 8. Mean error (ME) and Hausdorff distance (HD) due to the projection in the sub-space of modes reported in function of the number of modes for the L1 vertebra. The errors are evaluated with respect to the morphed mesh (A) and the original mesh (B) for the leave-one-out experiment. The dotted lines show the optimal number of modes. The shaded region represents the standard deviation. The standard deviation was about zero for the errors evaluated on the learning data.

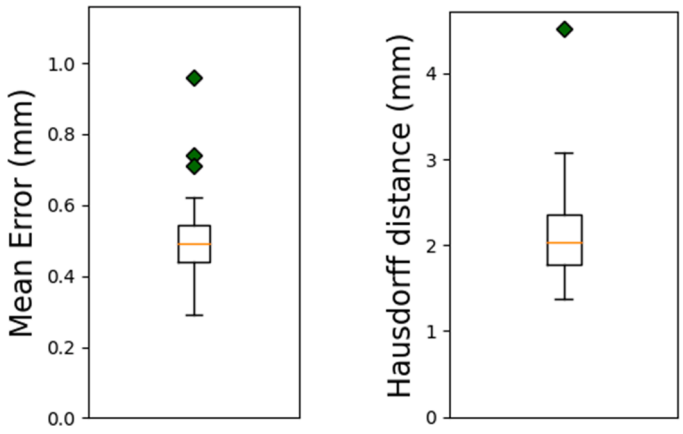

Fig. 9. Boxplots of the Mean Error (mm) and Hausdorff distance (mm). Mean values are provided in Table 4.

fact, data did not satisfy at least one of the two requisites. Therefore, to compare three groups of data (for all analyses mentioned above), statistical paired analyses were conducted with Friedman test (non-parametric). For significant differences, a Nemenyi Post-hoc test was performed. To compare two groups of data (for all analyses mentioned above), statistical paired analyses were conducted with paired *t*-test (parametric) and Wilcoxon signed-rank test (non-parametric). Significance level was considered at 0.05.

3. Results

3.1. Mesh morphing

The mean error and HD between the morphed mesh and the original geometries are reported in Table 3. The average, minimum and maximum errors are reported for each vertebral level and for all geometries in the dataset.

Overall, on the three levels, the average mean error was lower than 0.15 mm, showing an excellent reconstruction of the geometry of each patient through the mesh morphing process. Mean errors for L1 were lower than those for T12 (−3.7% difference, $p = 0.008$) and lower than those for L2 (−5.2% difference, $p = 0.006$). The differences between the mesh morphing errors at different levels were in some cases statistically significant but lower than 6%. Non-significant differences were found among the average Hausdorff distances for the three vertebral levels ($p = 0.09$). Examples of spatial distributions of the error, in frontal and postero-lateral views, were reported for the patients with the highest (Patient #16, T12 level, Fig. 7A-B), lowest (Patient #14, L2 level, Fig. 7E-F) and average (Patient #5, L1 level, Fig. 7C-D) HD. In most cases the largest HD occurred at the posterolateral part of the vertebral body for the T12 vertebrae. Overall, the morphing mesh captured well the shape of the original geometries as it is demonstrated by large parts on the geometry with error inferior to 0.5 mm (Fig. 7). For the case with a HD close to the average, this error occurred at the level of the inferior endplate where Patient #5 presented a small osteophyte (see red arrow in Fig. 7D).

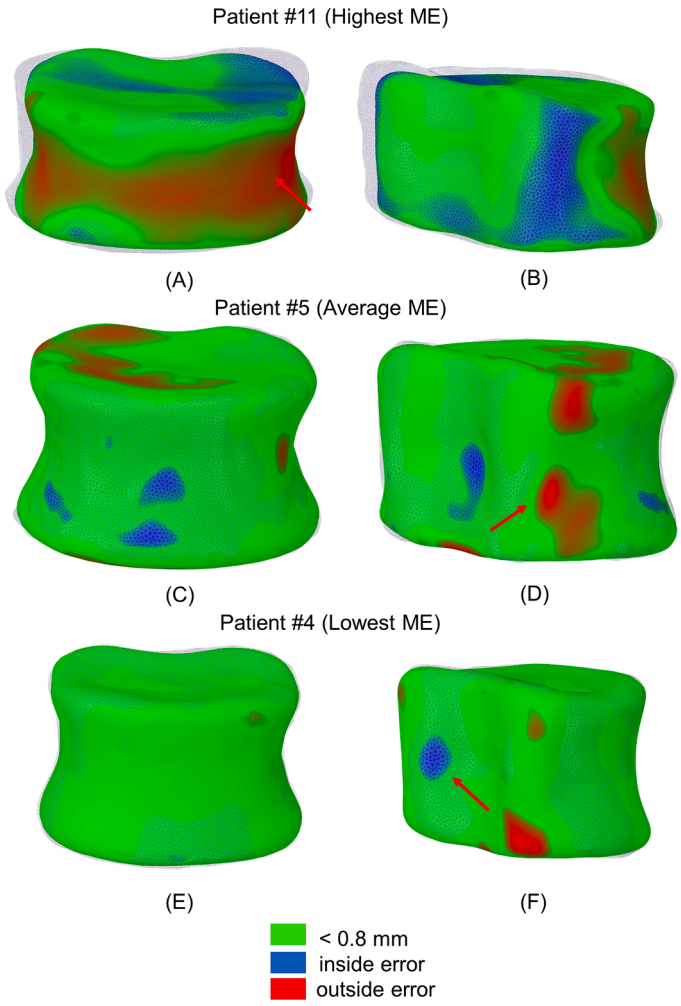

Fig. 10. Frontal and posterolateral views of the spatial distribution of the error between predicted and original meshes for the highest (A-B), average (C-D) and lowest (E-F) mean error (ME). Red arrows indicate the area where the Hausdorff distance (HD) occurred. The error is considered "inside" (blue) when the morphed mesh is inside the original one, and "outside" (red) when the morphed mesh is outside the original one.

3.2. Estimation of the optimal number of modes

The results are summarized in Fig. 8. The HD and mean errors evaluated on the left-out vectors and on all the learning vectors (mean value) are presented. The error evaluated with respect to the morphed meshes, which were used to build the matrix **H**, (Fig. 8A) and with respect to the original geometries (Fig. 8B) are reported. The trends of errors were very similar for L1 alone (Fig. 8) or if all the three vertebrae were considered (Appendix B).

As expected, the errors on left-out patients or on training data decreased when the number of modes increased. Considering the mean error on the left-out patient (morphed mesh, Fig. 8A), the error corresponding to 6 modes was lower than the error corresponding to 2 modes by 57%. Whereas, increasing the number of modes from 6 to 39 further reduced the error by 25%. An optimal number of modes equal to 6, corresponding to a mean error of 0.44 mm that is close to the voxel size of the best CT-scan (0.45 mm), was chosen. A similar behavior was observed for the HD: the error corresponding to 6 modes was lower than the error corresponding to 2 modes by 35%. When increasing the number of modes from 6 to 39 modes the HD decreased by 19%. An optimal number of modes equal to 6, corresponding to a HD of 1.75 mm and mean error of 0.44 mm, was chosen.

Table 4
Mean error and Hausdorff distance (HD) (mm) between the predicted 3D shape of L1 and the original or morphed geometry, as a function of the information used for the prediction. * represents a significant difference in the mean error or in the HD for the cases where data for T12 alone or L2 alone were used compared to the case where data from both T12 and L2 were used.

Reconstruction error with respect to the original geometry				
Level(s) used	Mean error (mm)		Hausdorff distance (mm)	
	Average ± st dev	(Min, Max)	Average ± st dev	(Min, Max)
T12 and L2	0.51 ± 0.11	(0.29, 0.96)	2.11 ± 0.56	(1.38, 4.52)
T12	*0.56 ± 0.13	(0.34, 1.09)	*2.31 ± 0.52	(1.45, 4.42)
L2	*0.55 ± 0.13	(0.32, 0.94)	2.22 ± 0.57	(1.36, 4.60)
Reconstruction error with respect to the morphed geometry				
	Mean error (mm)		Hausdorff distance (mm)	
Level(s) used	Average ± st dev	(Min, Max)	Average ± st dev	(Min, Max)
T12 and L2	0.49 ± 0.12	(0.26, 0.94)	1.88 ± 0.54	(1.23, 4.06)
T12	*0.54 ± 0.13	(0.32, 1.08)	*2.13 ± 0.49	(1.33, 3.96)
L2	*0.53 ± 0.13	(0.30, 0.92)	1.99 ± 0.55	(1.21, 4.15)

3.3. Prediction of the shape of L1

The results of the leave-one-out cross validation show that the mean reconstruction error of the 3D shape of L1 was on average 0.51 mm, and the HD was on average 2.11 mm (Fig. 9). Examples of error maps, in frontal and posterolateral views, are reported for the patient with the highest (mean error 0.96 mm, Patient #11 Fig. 10A-B), close to the average (mean error 0.51 mm, Patient #5, Fig. 10C-D), and lowest (mean value 0.29 mm, Patient #4, Fig. 10E-F) mean error.

Patient #35 and Patient #11 were associated with the lowest (1.38 mm) and highest (4.52 mm) values of HD, respectively. When the information about T12 alone was used to solve the minimization problem, the mean error and the HD increased by 10% ($p = 0.001$) and 9% ($p = 0.001$), respectively (Table 4); when the information about L2 alone was used, the mean error increased by 8% ($p = 0.012$) but the HD was not significantly different ($p = 0.074$) (Table 4). The mean error and the HD when using T12 alone or L2 alone were not statistical different ($p = 0.750$ and $p = 0.280$, respectively).

As expected the mean error (3.8%, $p < 0.001$) and the HD (10.5%, $p < 0.001$) evaluated on the original meshes were significantly higher than the case where the errors were evaluated on the morphed meshes (Table 4). The mean error ($p = 0.301$) and the HD ($p = 0.248$) evaluated on the morphed meshes (Table 4) were similar to the projection errors for the number of modes (6) used to predict the shape of the L1 vertebral body (Fig. 8A).

For Patient #4 (lowest mean error), the distribution of height across the vertebral body predicted for the L1 vertebral body was very similar to the distribution of the original geometry (Fig. 11E-F, Fig. 12C). For Patient #5 (average mean error) and for Patient #11 (highest mean error) the height of the vertebral body was overestimated (difference between median values equal to 1.05 mm) (Fig. 11C-D, Fig. 12B) or underestimated (difference between median values equal to −1.41 mm) (Fig. 11A-B, Fig. 12A), respectively. For this sub-group of patients, the difference between sagittal and frontal angles measured on original or predicted geometry was always lower than 1.8° and 1.4°, respectively.

For the testing dataset of 5 patients, the mean reconstruction error of the 3D shape of L1 was on average 0.65 ± 0.10 mm (range: 0.51–0.83 mm), and the HD was on average 3.54 ± 1.03 mm (range: 2.35–5.00 mm) (Fig. 13). The mean difference in median height between the

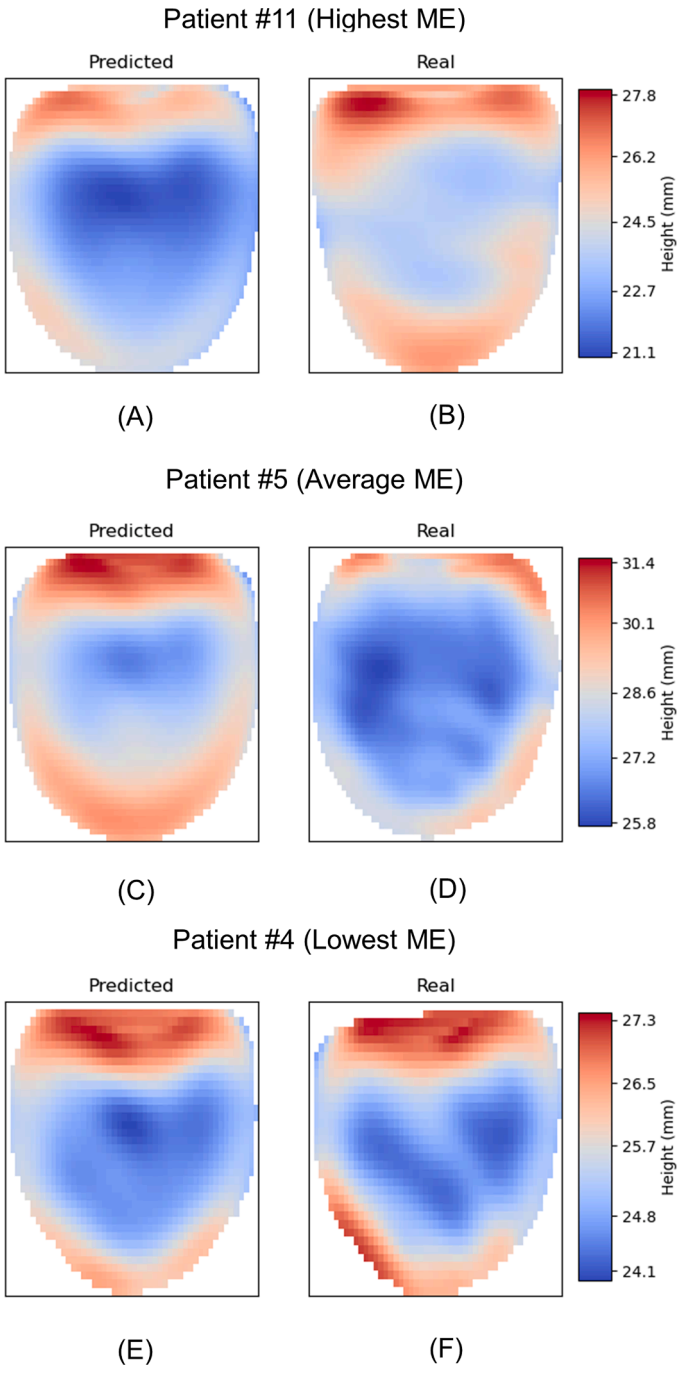

Fig. 11. Comparison of the maps of the distribution of heights of the vertebral bodies between predicted (A-C-E) and original meshes (B-D-F). The comparison is done for the best prediction case (A-B), an average one (C-D) and the worst one (E-F) with respect to the mean error (ME).

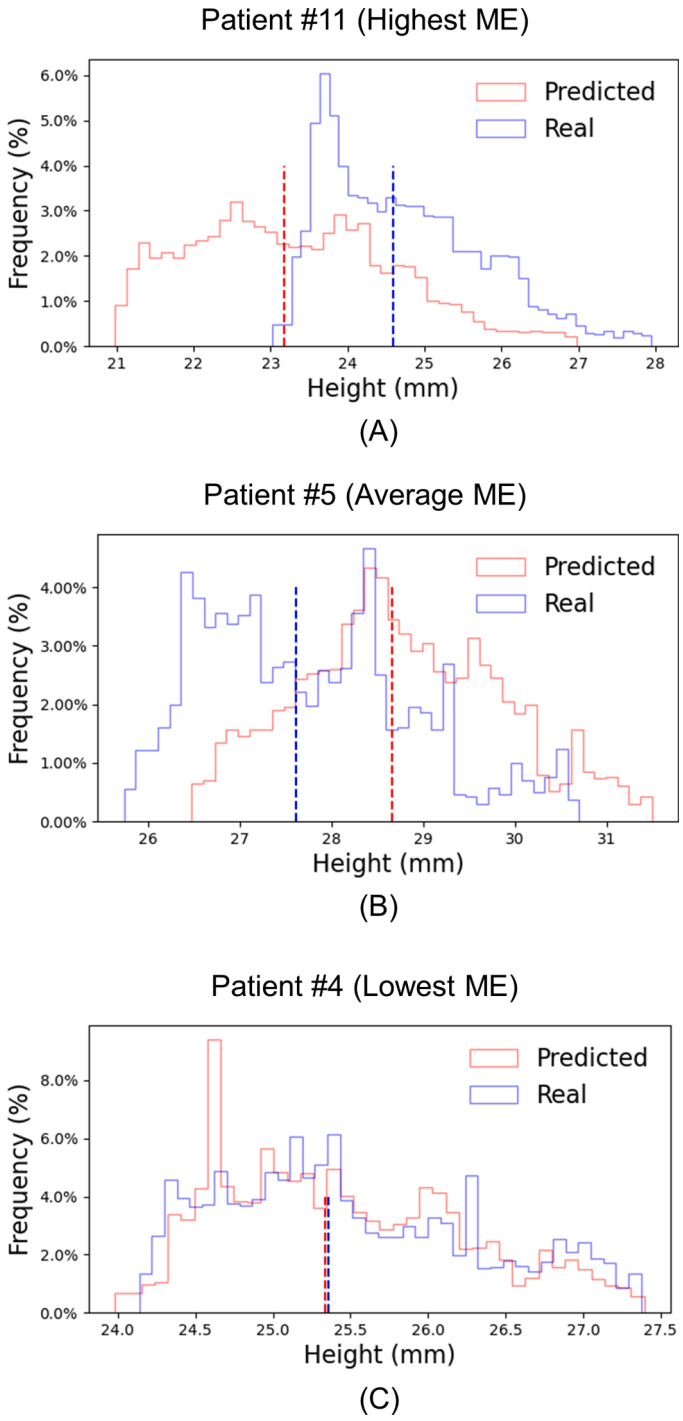

Fig. 12. Frequency plots of the heights of the predicted and real vertebral bodies for the worst prediction case (A), an average one (B) and the best one (C) with respect to the mean error (ME). Dotted lines represent the median values of distributions.

predicted and real vertebral bodies was 0.25 ± 0.19 mm. The distribution of height across the vertebral body was similar for predicted and real geometry apart from Patient #44 and Patient #45 that presented some differences over the endplates. The difference between sagittal and frontal angles measured on original or predicted geometry was 1.4° ± 1.0° (range: 0.49°−3.04°) and 0.6° ± 0.2° (range: 0.41°−0.89°), respectively.

3.4. Comparison with simpler approach

When the L1 vertebral body shape was approximated with the T12 shape, the mean error and the HD increased by 55% ($p < 0.001$) and 35% ($p < 0.001$) for the dataset for model construction and by 36% ($p < 0.001$) and 25% ($p < 0.001$) for the independent dataset, respectively (Table 5); when the L1 vertebral body shape was approximated with the L2 shape, the mean error and the HD increased by 35% and 32% for the dataset for model construction and by 40% and 20% for the independent dataset, respectively (Table 5).

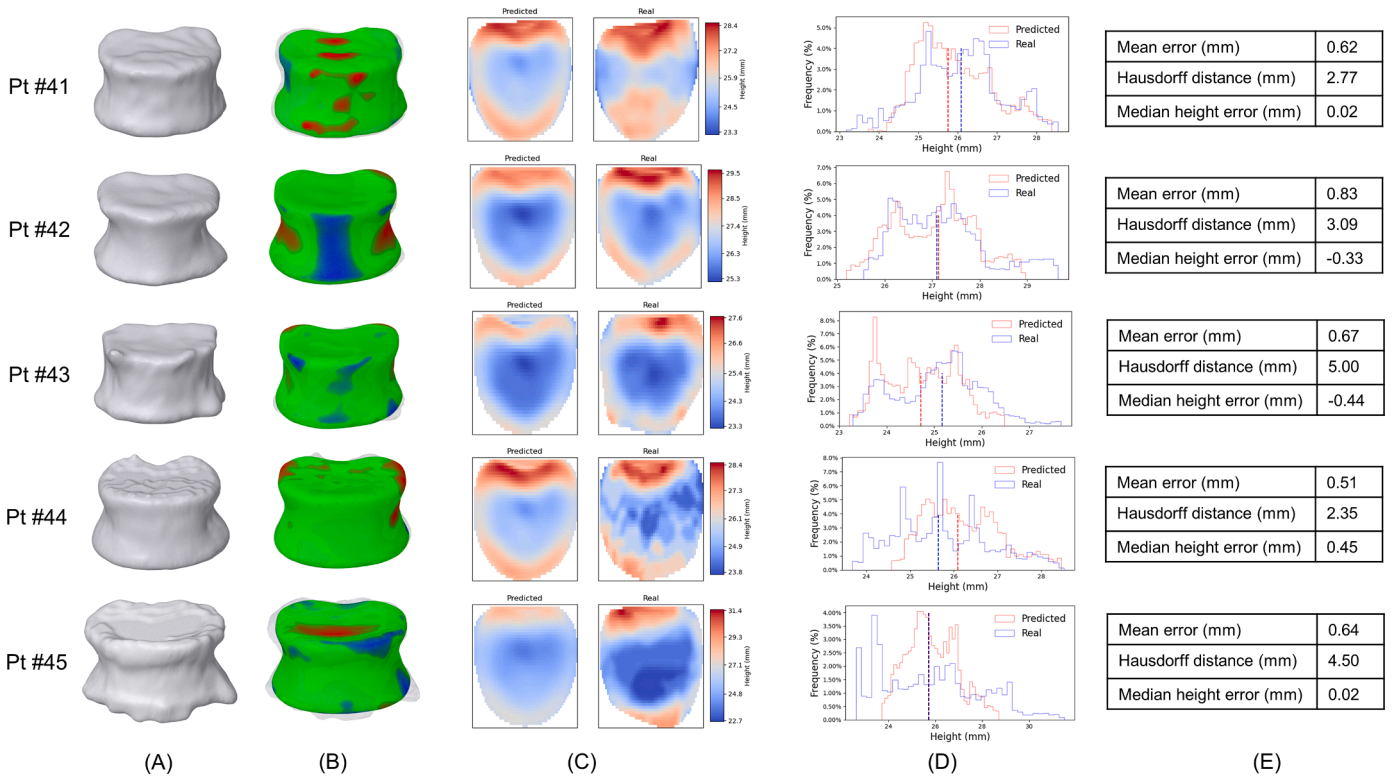

Fig. 13. Evaluation of the prediction of the shape of L1 for the testing dataset. Frontal view of the original geometry (A). Frontal view of the spatial distribution of the error between predicted and original meshes (B) (green corresponds to a distance lower than 0.8 mm, blue means that the morphed mesh is inside the original one, red means that the morphed mesh is outside the original one). Maps of the distribution of heights of the vertebral bodies (C). Frequency plots of the heights (D). Values of errors (E).

Table 5
Mean error and Hausdorff distance (HD) (mm) between the predicted 3D shape of L1 and the original geometry, where the predicted 3D shape of L1 is calculated by the SSM based algorithm or approximated with the shape of T12 or L2 vertebral bodies. * represents a significant difference in the mean error or in the HD for the cases where L1 is approximated with T12 or L2 compared to the case where L1 was predicted with the SSM based algorithm.

Reconstruction error with respect to the original geometry (LOO dataset)				
Comparison	Mean error (mm)		Hausdorff distance (mm)	
	Average ± st dev	(Min, Max)	Average ± st dev	(Min, Max)
L1pred vs L1real	0.51 ± 0.11	(0.29, 0.96)	2.11 ± 0.56	(1.38, 4.52)
T12real vs L1real	*0.79 ± 0.11	(0.56, 1.02)	*3.29 ± 0.55	(2.11, 4.32)
L2real vs L1real	*0.69 ± 0.12	(0.37, 0.98)	*2.79 ± 0.67	(1.33, 4.06)
Reconstruction error with respect to the original geometry (testing dataset)				
	Mean error (mm)		Hausdorff distance (mm)	
Comparison	Average ± st dev	(Min, Max)	Average ± st dev	(Min, Max)
L1pred vs L1real	0.65 ± 0.10	(0.51, 0.83)	3.54 ± 1.03	(2.35, 5.00)
T12real vs L1real	0.89 ± 0.12	(0.74, 1.09)	4.15 ± 1.04	(2.84, 5.05)
L2real vs L1real	0.91 ± 0.12	(0.78, 1.08)	4.26 ± 1.83	(2.83, 7.56)

4. Discussion

The goal of this study was to develop and validate an approach to reconstruct the 3D shape of an L1 human vertebral body by using the shapes of adjacent T12 and L2 vertebral bodies. The algorithm uses as input the segmentation of the two adjacent vertebral bodies (namely T12 and L2) from a CT scan of the lumbar spine and, by using the reference vertebral body mesh, predicts the 3D shape of the L1 vertebral body. This approach could potentially enable the prediction of the pre-fracture shape or height of a fractured vertebra. The algorithm showed an excellent reconstruction error of 0.51 ± 0.11 mm (mean error) for a dataset of 40 healthy patients (highest input CT-scan resolution equal to $0.68\times0.68\times0.45$ mm^3). The reconstruction error was slightly worse for the independent dataset including patients with osteophytes and severe bone degeneration (mean error of 0.65 ± 0.10 mm). Nevertheless, the mean errors are close to the voxel size of the input CT images, highlighting the potential of this approach for different clinical applications. In particular, the mean errors are lower than the precision of segmentations that could be obtained in a clinical setting by O-arm images (Casiraghi et al., 2021).

The morphing algorithm applied to CT images allowed accurate descriptions of patient-specific geometries with a single template mesh. The average mean error and HD between the morphed meshes and their corresponding original geometries were lower than 0.15 mm and 1 mm, respectively. It is difficult to compare these values with the literature as in most cases the mesh morphing error associated with the creation of SSMs of different bones (e.g. mandible (Wang et al., 2021), skull (Fuessinger et al., 2018), scapular bone (Plessers et al., 2018; Salhi et al., 2020), acetabular bone (Vanden Berghe et al., 2017) and C2 vertebra (Clogenson et al., 2015)) has not been reported. Campbell and Petrella (2016) created an SSM of the lumbar spine (L1-L5) (training set of 18 specimens) using a subject-specific mesh morphing technique characterized by a Euclidean node to surface distance lower than 10^{-5} mm, i.e., a perfect matching between the morphed and original geometries. The mesh morphing algorithm was based on 1306 landmarks automatically identified by a script that took approximately 15 min to run per vertebra. While this error is much lower than the one we report, it has to be remarked that the mean error in this study is three times lower than the

Table A1
. Patient IDs and VerSe2020 IDs, voxel size, sex (M = man, W = woman), age and CT-scan used for the acquisition of images (CT-Scanner (2: Philips ICT; 3: Philips IQON, 4: Siemens Somatom AS+; 8 Siemens external; 9: GE external; 10 Toshiba external) (Löffler et al., 2020).

Patient #	Verse 2020 ID	In-plane resolution (mm x mm)	Slice thickness (mm)	Sex	Age (years)	CT-scanner
1	517	0.68×0.68	0.9	M	42	3
2	540	0.98×0.98	0.9	W	19	3
3	550	0.78×0.78	0.8	M	38	2
4	075	1 × 1	1	W	56.6	2
5	552	0.75×0.75	0.9	M	67	3
6	570	0.91×0.91	0.9	M	50	3
7	591	0.81×0.81	0.9	M	67	3
8	597	0.80×0.80	0.9	M	64	2
9	141	1 × 1	2	W	62.6	4
10	254	1 × 1	2	M	27.4	4
11	702	0.80×0.80	3	M	77	10
12	402	1 × 1	2	M	35.2	4
13	407	1 × 1	2	M	18.9	4
14	413	1 × 1	1	W	23	2
15	415	1 × 1	2	M	34.8	4
16	500	0.68×0.68	0.90	M	35	3
17	708	0.78×0.78	0.80	W	50	10
18	521	0.68×0.68	1	W	35	7
19	532	0.93×0.93	0.6	M	23	4
20	533	0.72×0.72	0.6	M	41	4
21	508	0.988×0.98	0.70	M	39	4
22	522	0.73×0.73	0.9	W	71	3
23	529	0.68×0.68	0.9	W	20	3
24	547	0.92×0.92	0.9	W	24	3
25	763	1.07×1.07	3	M	19	9
26	554	0.92×0.92	0.9	M	70	3
27	805	0.73×0.73	0.7	W	44	8
28	569	0.73×0.73	0.9	W	46	3
29	573	0.98×0.98	0.9	W	37	2
30	576	0.78×0.78	0.9	W	36	3
31	580	0.76×0.76	0.9	M	27	3
32	606	0.68×0.68	0.45	W	58	3
33	609	0.68×0.68	0.9	M	31	3
34	502	0.98×0.98	0.6	W	35	4
35	618	0.98×0.98	0.9	M	28	2
36	627	0.78×0.78	0.9	W	47	3
37	636	0.75×0.75	0.9	W	42	3
38	703	0.66×0.66	0.8	M	32	10
39	753	0.83×0.83	2.5	W	28	9
40	761	1.31×1.31	3	M	36	9
41	96	1 × 1	1	W	60	2
42	553	0.68×0.68	0.9	W	60	3
43	616	0.72×0.72	0.9	W	77	3
44	711	0.72×0.72	0.8	M	62	10
45	814	0.33×0.33	0.9	M	77	8

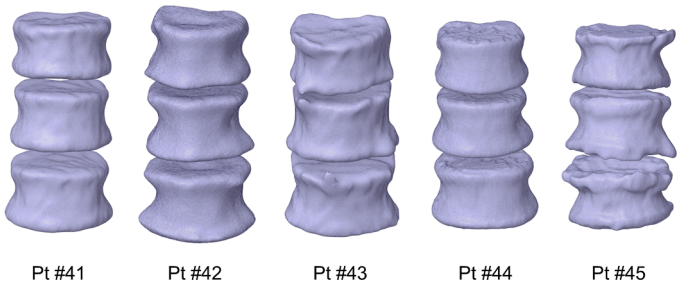

Fig. A1. Geometries of patients included in the external dataset. Patients #42, #43 and #45 presented severe bone degeneration and large osteophytes.

voxel size of the CT-scan with the best resolution in the dataset ($0.68\times0.68\times0.45$ mm^3), and therefore lower than the segmentation error. In addition, the HD was concentrated in small areas of the vertebral bodies not critical for the proposed application (e.g. at the posterolateral region of the vertebral body), or at the level of small protuberances or porosities that affect the anatomy of a limited number of patients. The mesh morphing error could be reduced by choosing a different kernel in the deformable morphing algorithm that would improve the retrieval of small details of geometries. However, a further reduction of the mesh morphing error would not make a significant impact on the description of the shapes, which were accurately captured by the morphing algorithm used in this study, and ultimately is not expected to influence the performance of the algorithm.

The optimal number of modes to build the minimization problem and to predict the shape of the L1 vertebral body was determined by repeating a leave-one-out experiment for all possible numbers of modes, end evaluating the projection error of patients external to the basis. This parameter has to be chosen based on the desired accuracy of the representation, and on the compromise of representing the variability of the training data without overfitting it (Brunton et al., 2016). For a SSM-based reconstruction of the scapular bone, Salhi et al. (2020) retained the first 15 modes that allowed to account for 95% of the variability in a training set of 82 samples. This approach is frequently used in literature, but it does not consider the ability to represent data outside the training set. By using the leave-one-out approach, the ability of the model to represent data which is not part of the training set is measured, and, therefore, this approach was preferred in this study. As expected, the mean and HDs on the training data approached zero when increasing the number of modes. The errors evaluated on the left-out patients with respect to the original meshes were slightly higher than the errors with respect to the morphed meshes while presenting similar trends. In fact, the error with respect to the original mesh could be interpreted as the combination of the mesh morphing error and the projection error. For this reason, the mean error and HD on the training data converged to a residual error which was dominated by the mesh morphing error.

In this study, the 3D shape of the L1 vertebral body was predicted with a mean error of 0.51 ± 0.11 mm and HD of 2.11 ± 0.56 mm, on average over the 40 patients in the construction dataset. The algorithm performed slightly worse for an external dataset containing older patients with large osteophytes and severe bone degeneration (mean error of 0.65 ± 0.10 mm and HD of 3.54 ± 1.03 mm, on average). For this dataset, the mean difference in median height between the predicted and real vertebral bodies was 0.25 ± 0.19 mm showing that the algorithm could also be used for an estimation of the median vertebral height, even though the differences may be higher locally over the endplates. While it is hard to identify an acceptable accuracy of the approach as it will depend on the different clinical applications, the approach, being based on the segmentation of CT images, is likely to be affected by their resolution. Nevertheless, the mean reconstruction error was lower to the precision associated with the detection of the contour of the vertebra in clinical protocols using O-arm imaging (resolution of ~0.4 mm), an advanced imaging system combining 2D and 3D acquisition modes which is often used in the operating room during spinal surgical procedures (Zhang et al., 2009). The mean error was also relatively small in comparison with the lowest dimension of the vertebrae in the dataset which was about 25 mm on average (vertebral height). The highest errors were associated with the worst voxel dimensions (e.g., slice thickness equal to 3 mm for Patient #11) or with the most degenerated shapes (Patient #42, Patient #43, Patient #45). The reconstruction errors were close to the projection errors obtained with the number of modes retained to compute the prediction (mean error of 0.44 ± 0.09 mm and HD of 1.75 ± 0.50 mm). As the projection errors represent the lowest reconstruction errors that could be found through the optimization process, the optimization showed excellent results and the reconstruction error may be further decreased by increasing the number of modes. In previous studies on SSM-based reconstruction of bones with artificial defects, the mean reconstruction error was 0.47 mm for the skull (node-to-node average distance) (Fuessinger et al., 2018), ~1 mm for the acetabular bone (mean Euclidean point to mesh distance equal to 1.2 ± 0.9 mm) (Vanden

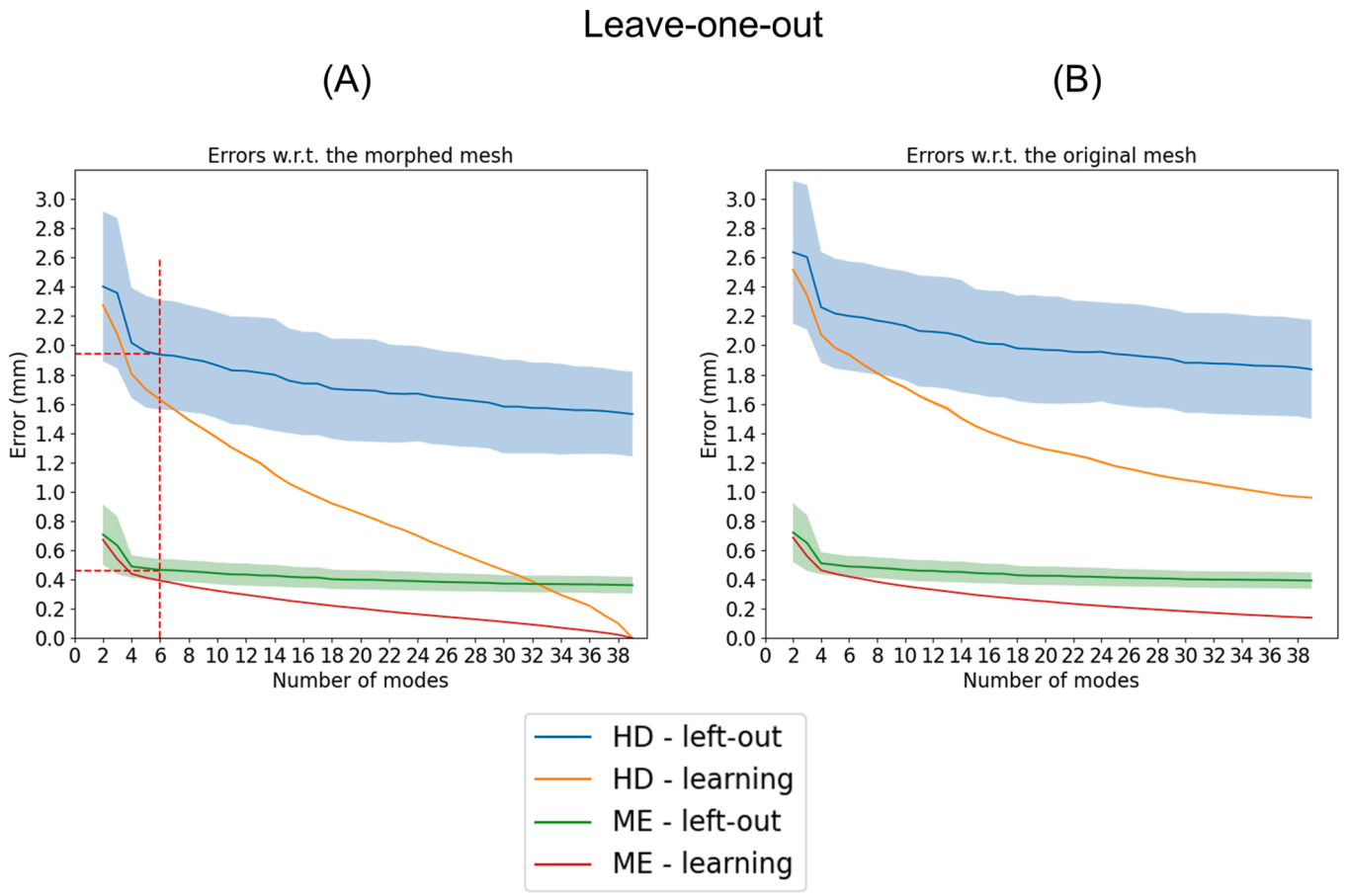

Fig. B1. Mean error (ME) and Hausdorff distance (HD) due to the projection in the sub-space of modes reported in function of the number of modes as average value for the T12, L1 and L2 vertebrae. The errors are evaluated with respect to the morphed mesh (A) and the original mesh (B) for the leave-one-out experiment. The dotted lines show the optimal number of modes. The shaded region represents the standard deviation. The standard deviation was about zero for the errors evaluated on the learning data.

Berghe et al., 2017) and scapula (root mean square error equal to 1.2 ± 0.4 mm (Plessers et al., 2018); mean closest point distance equal to 0.97 ± 0.14 mm (Salhi et al., 2020)). For the scapula Salhi et al. (2020) and Wang et al. (2021) reported average Hausdorff reconstruction distance of 5.86 ± 2.21 mm and 4.51 ± 2.65 mm, respectively. The prediction errors observed in the present study were similar to those reported in Fuessinger et al., 2018 and lower than those reported in Vanden Berghe et al. (2017), Plessers et al. (2018), Salhi et al. (2020) and Wang et al. (2021). The differences between these studies could be due to the different studied anatomical sites (vertebrae vs scapula or pelvis), reconstruction approaches (T12 and L2 vertebral bodies to reconstruct the L1 vertebral body vs reconstruction of bones with artificial defects from healthy bones), and distance metrics. In a simpler 2D case, de Bruijne et al. (2007) found a mean distance (closest point distance) between the original and reconstructed shapes of unfractured vertebrae equal to 0.8 ± 0.4 mm, which is higher than the mean distance found in the present study on the 3D shape of the vertebral body. Moreover, in that study, the error increased for L1 and L4 levels if only one adjacent vertebra was used as input. This is in line with the findings of the present study, which showed higher errors of about 10% if the information of only one adjacent vertebra was used as input. Significant differences were found between the reconstruction errors obtained by this approach and a simpler method that uses the segmented shapes of T12 or L2 vertebral bodies. Although the algorithm provided better performance, the clinical impact of the method has to be demonstrated (e.g. biomechanical studies based on Finite Element models). In fact, differences between the two approaches were on average below the voxel size, highlighting that in most cases where the height of the vertebral body has to be estimated for a certain surgical procedure using the simpler approach based on the segmentations of the adjacent vertebrae would probably be accurate enough. Nevertheless, the improvements in estimating the shape of the vertebral bodies (max difference in mean error of 0.6 mm (Patient #6) and in HD of 2.56 mm (Patient #43)) suggests that this approach can be helpful in some cases. Similar considerations may be applied to studies on the acetabular bone (Vanden Berghe et al., 2017) and pelvis (Krol et al., 2013) that showed an improvement in the estimation of hip joint center of 0.4 mm (on average) and in the reconstruction mean distance of 0.26 mm (on average), respectively, if the contralateral bone was used as a template for the reconstruction.

This study has some limitations. First, the performance of the algorithm was slightly worse for older patients with large osteophytes than for healthy patients. However, the approach could be adapted to better predict shapes of L1 in case of specific pathologies by using training datasets specific for each application. Second, this method has been assessed only on the vertebrae at the thoracolumbar junction (T12, L1 and L2). While the thoracolumbar junction is the area where traumatic fractures of the spine occur more often (Bensch et al., 2005; Wood et al., 2014), probably due to the sudden change in curvature and stiffness resulting in a concentration of biomechanical stress (Oxland et al., 1992), the approach presented in this study can be extended to other lumbar and lower thoracic vertebral bodies. This would be particularly useful in cases where more vertebrae adjacent to the investigated one are also affected by fractures. In fact, we expect a degradation of the quality of the prediction in cases where the adjacent vertebrae also present signs of fractures or microfractures, as showed by de Bruijne et al. (2007). Nevertheless, the approach can be extended in the future to

predict the shape of a vertebra based on the geometry of non-adjacent levels, with likely the need to accept lower accuracy. In these cases, the performance of the algorithm is expected to be significantly better than simpler approaches based on direct approximation of one vertebra shape with the most adjacent one. Additionally, this method focused only on the prediction of the shape of the vertebral body. The approach could be adapted to study the shape of the posterior part of the spine, which however are generally associated with high-energy trauma and neurologic injury (Magerl et al., 1994; Wood et al., 2014). Finally, the extraction of vertebral bodies from segmentations and the placement of anatomical landmarks were executed with a manual procedure as well as the definition of vertebral endplates for the estimation of vertebral angles. The intra- and inter- operator reproducibility of these steps need to be assessed before clinical application of the methodology.

In conclusion, in this study a methodology to predict the 3D shape of the L1 vertebral body from adjacent ones was developed and validated. This research could lead to practical application as the pre-fracture 3D shape of the vertebral body could be used by surgeons to choose the optimal treatment to restore the anatomy of the vertebra and to optimize the reduction of vertebral fractures in multiple anatomical planes (Aebi, 2007).

Funding

This project was partially funded by the European Union's Horizon 2020 research and innovation program under the Marie Skłodowska-Curie grant agreement Spinner No. 766,012, and by the Engineering and Physical Sciences Research Council (EPSRC) Frontier Multisim Grant (EP/K03877X/1 and EP/S032940/1).

CRediT authorship contribution statement

M. Sensale: Conceptualization, Methodology, Software, Formal analysis, Data curation, Writing – original draft, Visualization, Writing – review & editing. **T. Vendeuvre:** Conceptualization, Writing – review & editing. **A. Germaneau:** Conceptualization, Writing – review & editing. **C. Grivot:** Methodology, Writing – review & editing. **M. Rochette:** Conceptualization, Methodology, Validation, Writing – review & editing, Supervision. **E. Dall'Ara:** Conceptualization, Methodology, Validation, Writing – review & editing, Supervision.

Declaration of Competing Interest

The authors declare the following financial interests/personal relationships which may be considered as potential competing interests. Marco Sensale reports financial support was provided by Ansys Inc. Christelle Grivot reports financial support was provided by Ansys Inc. Michel Rochette reports financial support was provided by Ansys Inc.

Data availability

The data and code supporting the conclusions of this article is available at: https://doi.org/10.15131/shef.data.22561375. The code to perform the reconstruction, as well the modes extracted by SVD are shared. The SVD was done with an in-house Ansys proprietary code, which cannot be shared.

Acknowledgments

The authors gratefully acknowledge the organizers of the VerSe2020 challenge for publishing the CT spine dataset and Kévin Aubert for software support.

Appendix A. Table of correspondence between patient IDs and Verse 2020 IDs

Table A1 and Fig. A1

Appendix B. Projection errors averaged over the T12, L1 and L2 vertebrae

Fig. B1

References

Aebi, M., 2007. AOSpine Manual. AOSpine International.

Bensch, F.V., Koivikko, M.P., Kiuru, M.J., Koskinen, S.K., 2005. The incidence and distribution of burst fractures. Emerg. Radiol. 12, 124. https://doi.org/10.1007/s0010140-005-0457-5.

Brunton, A., Salazar, A., Bolkart, T., Wuhrer, S., 2016. Statistical shape spaces for 3d data: a review, in: handbook of Pattern Recognition and Computer Vision. World scientific 217–238. https://doi.org/10.1142/9789814656535_0012.

Campbell, J.Q., Petrella, A.J., 2015. An automated method for landmark identification and finite-element modeling of the lumbar spine. IEEE Trans. Biomed. Eng. 62, 2709–2716. https://doi.org/10.1109/TBME.2015.2444811.

Campbell, J.Q., Petrella, A.J., 2016. Automated finite element modeling of the lumbar spine: using a statistical shape model to generate a virtual population of models. J. Biomech. 49, 2593–2599. https://doi.org/10.1016/j.jbiomech.2016.05.013.

Casiraghi, M., Scarone, P., Bellesi, L., Piliero, M.A., Pupillo, F., Gaudino, D., Fumagalli, G., Grande, F., Presilla, S., 2021. Effective dose and image quality for intraoperative imaging with a cone-beam CT and a mobile multi-slice CT in spinal surgery: a phantom study. Phys. Med. 81, 9–19. https://doi.org/10.1016/j.ejmp.2020.11.006.

Clogenson, M., Duff, J.M., Luethi, M., Levivier, M., Meuli, R., Baur, C., Henein, S., 2015. A statistical shape model of the human second cervical vertebra. Int. J. Comput. Assist. Radiol. Surg. 10, 1097–1107. https://doi.org/10.1007/s11548-014-1121-x.

Commandeur, F., Velut, J., Acosta, O., 2011. A VTK Algorithm for the Computation of the Hausdorff Distance. VTK J., 2011 January-December Submissions 839.

Day, G.A., Jones, A.C., Wilcox, R.K., 2022. Using Statistical Shape and Appearance Modelling to characterise the 3D shape and material properties of human lumbar vertebrae: a proof of concept study. J. Mech. Behav. Biomed. Mater. 126, 105047 https://doi.org/10.1016/j.jmbbm.2021.105047.

de Bruijne, M., Lund, M.T., Tankó, L.B., Pettersen, P.C., Nielsen, M., 2007. Quantitative vertebral morphometry using neighbor-conditional shape models. Med. Image Anal. In: Special Issue on the Ninth International Conference on Medical Image Computing and Computer-Assisted Interventions - MICCAI, pp. 503–512. https://doi.org/10.1016/j.media.2007.07.004, 2006 11.

Fedorov, A., Beichel, R., Kalpathy-Cramer, J., Finet, J., Fillion-Robin, J.-C., Pujol, S., Bauer, C., Jennings, D., Fennessy, F., Sonka, M., Buatti, J., Aylward, S., Miller, J.V., Pieper, S., Kikinis, R., 2012. 3D Slicer as an image computing platform for the Quantitative Imaging Network. Magn. Reson. Imaging, Quantitative Imaging in Cancer 30, 1323–1341. https://doi.org/10.1016/j.mri.2012.05.001.

Fuessinger, M.A., Schwarz, S., Cornelius, C.-P., Metzger, M.C., Ellis, E., Probst, F., Semper-Hogg, W., Gass, M., Schlager, S., 2018. Planning of skull reconstruction based on a statistical shape model combined with geometric morphometrics. Int. J. Comput. Assist. Radiol. Surg. 13, 519–529. https://doi.org/10.1007/s11548-017-1674-6.

Genant, H.K., Wu, C.Y., van Kuijk, C., Nevitt, M.C., 1993. Vertebral fracture assessment using a semiquantitative technique. J. Bone Miner. Res. Off. J. Am. Soc. Bone Miner. Res. 8, 1137–1148. https://doi.org/10.1002/jbmr.5650080915.

Graphics and Vision Research group, University of Basel, 2020. Scalismo - Scalable Image Analysis and Shape Modelling. https://github.com/unibas-gravis/scalismo (accessed 21.8.22).

Grazier, K., Holbrook, T.L., Kelsey, J.L., et al., 1984. The frequency of occurrence, impact, cost of selected musculoskeletal conditions in the United States. Am Acad Orthop Surg.

Hollenbeck, J.F.M., Cain, C.M., Fattor, J.A., Rullkoetter, P.J., Laz, P.J., 2018. Statistical shape modeling characterizes three-dimensional shape and alignment variability in the lumbar spine. J. Biomech. 69, 146–155. https://doi.org/10.1016/j.jbiomech.2018.01.020.

Kirschke, J.S., Löffler, M., Sekuboyina, A., 2020. Verse 2020. https://osf.io/t98fz/ (accessed 21.8.22).

Krol, Z., Skadlubowicz, P., Hefti, F., Krieg, A.H., 2013. Virtual reconstruction of pelvic tumor defects based on a gender-specific statistical shape model. Comput. Aided Surg. Off. J. Int. Soc. Comput. Aided Surg. 18, 142–153. https://doi.org/10.3109/10929088.2013.777973.

Liebl, H., Schinz, D., Sekuboyina, A., Malagutti, L., Löffler, M.T., Bayat, A., Husseini, M. E., Tetteh, G., Grau, K., Niederreiter, E., Baum, T., Wiestler, B., Menze, B., Braren, R., Zimmer, C., Kirschke, J.S., 2021. A computed tomography vertebral segmentation dataset with anatomical variations and multi-vendor scanner data. ArXiv210306360 Cs Eess.

Lin, C.-C., Wen, S.-H., Chiu, C.-H., Chen, I.-H., Yu, T.-C., 2009. The clinical influence of fluid sign in treated vertebral bodies after percutaneous vertebroplasty. Radiology 251, 866–872. https://doi.org/10.1148/radiol.2513080914.

Löffler, M.T., Sekuboyina, A., Jacob, A., Grau, A.-L., Scharr, A., El Husseini, M., Kallweit, M., Zimmer, C., Baum, T., Kirschke, J.S., 2020. A Vertebral Segmentation

Dataset with Fracture Grading. Radiol. Artif. Intell. 2, e190138 https://doi.org/10.1148/ryai.2020190138.
Luthi, M., Gerig, T., Jud, C., Vetter, T., 2018. Gaussian Process Morphable Models. IEEE Trans. Pattern Anal. Mach. Intell. 40, 1860–1873. https://doi.org/10.1109/TPAMI.2017.2739743.
Maestretti, G., Sutter, P., Monnard, E., Ciarpaglini, R., Wahl, P., Hoogewoud, H., Gautier, E., 2014. A prospective study of percutaneous balloon kyphoplasty with calcium phosphate cement in traumatic vertebral fractures: 10-year results. Eur. Spine J. 23, 1354–1360. https://doi.org/10.1007/s00586-014-3206-1.
Magerl, F., Aebi, M., Gertzbein, S.D., Harms, J., Nazarian, S., 1994. A comprehensive classification of thoracic and lumbar injuries. Eur. Spine J. 3, 184–201. https://doi.org/10.1007/BF02221591.
Noriega González, D.C., Ardura Aragón, F., Crespo Sanjuan, J., Santiago Maniega, S., Labrador Hernández, G., Bragado González, M., Pérez-Valdecantos, D., Caballero-García, A., Córdova, A., 2022. Restoration in vertebral compression fractures (vcf): effectiveness evaluation based on 3D technology. J. Funct. Biomater. 13, 60. https://doi.org/10.3390/jfb13020060.
Oxland, T.R., Lin, R.-.M., Panjabi, M.M., 1992. Three-Dimensional mechanical properties of the thoracolumbar junction. J. Orthop. Res. 10, 573–580. https://doi.org/10.1002/jor.1100100412.
Ortiz, A.O., Bordia, R., 2011. Injury to the vertebral endplate-disk complex associated with osteoporotic vertebral compression fractures. AJNR Am. J. Neuroradiol. 32, 115–120. https://doi.org/10.3174/ajnr.A2223.
Pereañez, M., Lekadir, K., Castro-Mateos, I., Pozo, J.M., Lazáry, Á., Frangi, A.F., 2015. Accurate segmentation of vertebral bodies and processes using statistical shape decomposition and conditional models. IEEE Trans. Med. Imaging 34, 1627–1639. https://doi.org/10.1109/TMI.2015.2396774.
Plessers, K., Berghe, P.V., Dijck, C.V., Wirix-Speetjens, R., Debeer, P., Jonkers, I., Sloten, J.V., 2018. Virtual reconstruction of glenoid bone defects using a statistical shape model. J. Shoulder Elbow Surg. 27, 160–166. https://doi.org/10.1016/j.jse.2017.07.026.
Roberts, M.G., Pacheco, E.M.B., Mohankumar, R., Cootes, T.F., Adams, J.E., 2010. Detection of vertebral fractures in DXA VFA images using statistical models of appearance and a semi-automatic segmentation. Osteoporos. Int. 21, 2037–2046. https://doi.org/10.1007/s00198-009-1169-6.
Salhi, A., Burdin, V., Boutillon, A., Brochard, S., Mutsvangwa, T., Borotikar, B., 2020. Statistical shape modeling approach to predict missing scapular bone. Ann. Biomed. Eng. 48, 367–379. https://doi.org/10.1007/s10439-019-02354-6.
Salle, H., Meynard, A., Auditeau, E., Gantois, C., Rouchaud, A., Mounayer, C., Faure, P., Caire, F., 2021. Treating traumatic thoracolumbar spine fractures using minimally invasive percutaneous stabilization plus balloon kyphoplasty: a 102-patient series. J. NeuroInterventional Surg. 13, 848–853. https://doi.org/10.1136/neurintsurg-2020-017238.
Schousboe, J.T., 2016. Epidemiology of vertebral fractures. J. Clin. Densitom. 19, 8–22. https://doi.org/10.1016/j.jocd.2015.08.004.
Schroeder, W., Martin, K., Lorensen, B., 2006. The visualization toolkit (4th ed.), Kitware.
Sekuboyina, A., Bayat, A., Husseini, M.E., Löffler, M., Li, H., Tetteh, G., Kukačka, J., Payer, C., Štern, D., Urschler, M., Chen, M., Cheng, D., Lessmann, N., Hu, Y., Wang, T., Yang, D., Xu, D., Ambellan, F., Amiranashvili, T., Ehlke, M., Lamecker, H., Lehnert, S., Lirio, M., de Olaguer, N.P., Ramm, H., Sahu, M., Tack, A., Zachow, S., Jiang, T., Ma, X., Angerman, C., Wang, X., Wei, Q., Brown, K., Wolf, M., Kirszenberg, A., Puybareauq, É., Valentinitsch, A., Rempfler, M., Menze, B.H., Kirschke, J.S., 2020. VerSe: A Vertebrae Labelling and Segmentation Benchmark for Multi-detector CT Images. ArXiv200109193 Cs Eess.
Vaccaro, A., Kandziora, F., Fehlings, M., Shanmughanathan, R., 2020. AO Spine Surgery Ref. https://surgeryreference.aofoundation.org/spine/trauma/thoracolumbar (accessed 21.8.22).
Van Meirhaeghe, J., Bastian, L., Boonen, S., Ranstam, J., Tillman, J.B., Wardlaw, D., 2013. A randomized trial of balloon kyphoplasty and nonsurgical management for treating acute vertebral compression fractures. Spine 38, 971–983. https://doi.org/10.1097/BRS.0b013e31828e8e22.
Vanden Berghe, P., Demol, J., Gelaude, F., Vander Sloten, J., 2017. Virtual anatomical reconstruction of large acetabular bone defects using a statistical shape model. Comput. Methods Biomech. Biomed. Engin. 20, 577–586. https://doi.org/10.1080/10255842.2016.1265110.
Verheyden, A.P., Spiegl, U.J., Ekkerlein, H., Gercek, E., Hauck, S., Josten, C., Kandziora, F., Katscher, S., Kobbe, P., Knop, C., Lehmann, W., Meffert, R.H., Müller, C.W., Partenheimer, A., Schinkel, C., Schleicher, P., Scholz, M., Ulrich, C., Hoelzl, A., 2018. Treatment of fractures of the thoracolumbar spine: recommendations of the spine section of the german society for orthopaedics and trauma (DGOU). Glob. Spine J. 8, 34S–45S. https://doi.org/10.1177/2192568218771668.
Wang, X.-.R., Xu, F.-.R., Huang, Q.-.L., Wáng, Y.X.J., 2020. Radiological features of traumatic vertebral endplate fracture: an analysis of 194 cases with 263 vertebral fractures. Chin. Med. J. (Engl.) 133, 2696–2702. https://doi.org/10.1097/CM9.0000000000000919.
Wang, E., Tran, K.L., D'heygere, E., Prisman, E., 2021. Predicting the premorbid shape of a diseased mandible. Laryngoscope 131, E781–E786. https://doi.org/10.1002/lary.29009.
Whitmarsh, T., Humbert, L., Del Río Barquero, L.M., Di Gregorio, S., Frangi, A.F., 2013. 3D reconstruction of the lumbar vertebrae from anteroposterior and lateral dual-energy X-ray absorptiometry. Med. Image Anal. 17, 475–487. https://doi.org/10.1016/j.media.2013.02.002.
Wood, K.B., Li, W., Lebl, D.S., Ploumis, A., 2014. Management of thoracolumbar spine fractures. Spine J 14, 145–164. https://doi.org/10.1016/j.spinee.2012.10.041.
Xu, Y., Goodacre, R., 2018. On splitting training and validation set: a comparative study of cross-validation, bootstrap and systematic sampling for estimating the generalization performance of supervised learning. J. Anal. Test. 2, 249–262. https://doi.org/10.1007/s41664-018-0068-2.
Yeung, S., Toor, A., Deib, G., Zhang, J., Besier, T., Fernandez, J., 2020. Relationship between lower lumbar spine shape and patient bone metabolic activity as characterised by 18F NaF bio-markers. Comput. Biol. Med. 116, 103529 https://doi.org/10.1016/j.compbiomed.2019.103529.
Zhang, J., Weir, V., Fajardo, L., Lin, J., Hsiung, H., Ritenour, E., 2009. Dosimetric characterization of a cone-beam O-arm (TM) imaging system. J. X-Ray Sci. Technol. 17, 305–317. https://doi.org/10.3233/XST-2009-0231.
Zheng, G., Nolte, L.-.P., Ferguson, S.J., 2011. Scaled, patient-specific 3D vertebral model reconstruction based on 2D lateral fluoroscopy. Int. J. Comput. Assist. Radiol. Surg. 6, 351–366. https://doi.org/10.1007/s11548-010-0515-7.